Master's thesis

NTNU
Norwegian University of Science and Technology
Faculty of Natural Sciences
Department of Physics

Ahmad Chehaimi

Ultrafast Laser Direct Writing as a key enabling technology for silicon processing

A new target for positronium Bose-Einstein condensation and performance improvements of the MALTA2 tracking sensor

Master's thesis in Physics
Supervisor: Prof. Irina T. Sorokina, NTNU
Co-supervisor: Dr. Sebastiano Mariazzi, UNITN, and Dr. Florian Dachs, CERN

June 2024

NTNU
Norwegian University of Science and Technology

UNIVERSITÀ DI TRENTO

CERN

Ahmad Chehaimi

Ultrafast Laser Direct Writing as a key enabling technology for silicon processing

A new target for positronium Bose-Einstein condensation and performance improvements of the MALTA2 tracking sensor

Master's thesis in Physics
Supervisor: Prof. Irina T. Sorokina, NTNU
Co-supervisor: Dr. Sebastiano Mariazzi, UNITN, and Dr. Florian Dachs, CERN
June 2024

Norwegian University of Science and Technology
Faculty of Natural Sciences
Department of Physics

NTNU
Norwegian University of
Science and Technology

Ahmad Chehaimi

Ultrafast Laser Direct Writing as a key enabling technology for silicon processing:

A new target for positronium Bose-Einstein condensation, and tracking sensor MALTA2 performance improvements

Master's thesis in Physics

Supervisor: Prof. I. T. Sorokina, NTNU

Co-supervisors: Dr. S. Mariazzi, UNITN, and Dr. F. Dachs, CERN

June 2024

Norwegian University of Science and Technology

Faculty of Natural Sciences

Department of Physics

NTNU

Contents

Abstract

In the present work we show two applications of a laser processing technique called Ultrafast Laser Direct Writing (ULDW). In-bulk modifications can be induced in a crystalline semiconductor to control its solid state and optical properties. The laser induced modifications have been characterized in silicon with Positron Annihilation Spectroscopy (PAS), that showed a high density of lattice defects and vacancies. In addition, the modified volume showed a high etching selectivity compared to the unprocessed silicon, upon use of HF-based etchants. The reported qualities have been fundamental for the successful production of a target designed for the synthetization of a Bose-Einstein condensate of positronium (the bound state between an electron and a positron), where embedded hollow cavities connected to the surface by a comb of nanochannels were produced in a silicon wafer. The second application involved ULDW to improve the sensitivity of the silicon-based Depleted Monolithic Active Pixel Sensor MALTA2. The idea was to introduce controlled laser modifications in the depletion layer of the chip to shape the electric field gradient, and fasten the signal collection. However, the metallized surface of MALTA2 did not allow full control of the laser processing by reflecting the beam, and no successful implantation was obtained. Lastly, Two Photon Absorption-Transient Current Technique (TPA-TCT) was used to characterize the charge collection capabilities of single pixels of MALTA2. TPA-TCT can be used to directly study electronic and solid state properties of the laser-induced defects, and the possibilities and limitations in shaping the depletion layer in silicon based chip.

Preface

The idea of this master thesis has been developed under the pulling forces of three poles: Norwegian University of Science and Technology (NTNU), University of Trento (UNITN), and European Organization for Nuclear Research (CERN). In the laboratories of NTNU, the Laser Group, under the supervision of Prof. Irina T. Sorokina, has extended a technique called Ultrafast Laser Direct Writing (ULDW) for processing of dielectrics to semiconductors, specifically for the induction of in-bulk modification of crystalline silicon. The in-bulk modification of a monocrystalline silicon presents certain challenges, and their solution allows the production and control of the laser-induced defects inside the silicon volume. Fine material processing of silicon, in general, presents challenges, especially, if such processing is carried out by pulsed commercial lasers operating slightly above 1 μm or even at 1.5 μm. This is due to a strong two-photon absorption in silicon at these wavelengths. In 2018 R. Richter et al. [1] have demonstrated that it is possible to overcome these challenges and have produced, for the first time, subsurface defects in monocrystalline silicon using picosecond and femtosecond pulses at wavelengths of 2 and 2.3 μm, correspondingly. For the first time, the authors of Ref. [1] have also shown that the combined effect of the two-photon absorption, three-photon absorption and second order nonlinearity lead to the existence of the optimum wavelength (around 2.1-2.2 μm) for subsurface processing of silicon. At this wavelength the multiphoton absorption is minimized and the effect from the third order nonlinearity is maximized, making it possible to concentrate with a single pulse a large amount of pulse energy in a tiny, sub-micron spot. This opened the way to a practical and repeatable single pulse sub-surface modification in silicon [2]. Before that, single-pulse modification was only reported in the middle of a silicon microsphere [3] or in a special interferometer configuration (a thin plane-parallel polished silicon wafer) where the effect of induced nonlinearity in the counterpropagating nanosecond laser beams played a major role [4], making it an unpractical method in an industrial setting. As a result of this work, an ultrashort pulsed laser for subsurface processing of semiconductors was developed to operate at a wavelength of 2.09 μm[2] [5], and com-

mercialized by an NTNU spinoff company ATLA Lasers AS. This technique is evidently a technology which can be used in numerous applications, and opened up opportunities in-volume 3D-processing of semiconductors, microelectronics as well as fundamental science. In this frame, UNITN and CERN's interest was captured envisioning its use in two interesting fundamental science projects.

On UNITN's side, the intuition was to use ULDW to accommodate, along with etching techniques, the formation of a subsurface hollow cavity connected to the surface by means of nanochannels. This is the description of the envisioned target for positronium production and accumulation. Such a target could pave the way to the fist Bose-Einstein condensate of a purely leptonic atom.

On CERN's side, ULDW was of interest to improve the performance of the MALTA2 silicon-based pixel sensor. The idea was to implant laser-induced defects in the crystalline structure of the chip to shape its depletion layer. A successful implantation would shorten the collection time of the free carries generated by ionising particles crossing the detector, improving the sensitivity and the overall detector performance.

In the work you are going to read, I will present the ideas born within a Large Scale Interdisciplinary NFR project "MIR" in frames of international collaboration between UNITN, CERN and NTNU "MIR" project partners, and their development into the final products showing the promising achievements and limitation of the application as well as the improvements that can be explored in future studies. The thesis is structured as follows: chapter 1 provides the theoretical basis behind the implemented ULDW technique for producing defects, chapter 2 describes the experimental setup used for writing the defects, chapter 3 and 4 describe the produced positronium target and the experiment, and chapter 5 reports the results with the MALTA chip, followed by the conclusion and outlook.

1. Ultrafast Laser Direct Writing

The fundamental effect of Ultrafast Laser Direct Writing (ULDW) is the localized in-bulk modification of a material transparent to the laser wavelength, while leaving the material untouched along the optical path traversed by the laser pulse. Although the material is transparent to the laser wavelength at low intensities[1], the laser energy can be absorbed by the material bulk due to optical non linearities that arise if high intensities are achieved.

The required high optical intensities for ULDW are obtained employing ultrafast pulsed lasers. The average power of the laser beam can be relatively low, but each pulse carries high energies. The pulse energy (E_{pulse}) and the average power (<P>) are related by the repetition rate of the pulse, i.e. the frequency with which the pulses are emitted:

$$E_{pulse} = \frac{< P >}{f_{rep}} \tag{1.1}$$

In addition, since the pulses are extremely short (with pulse width, τ, at least in the nanosecond range) and focused into a small area A, the peak intensity reaches extremely high values:

$$I_{peak} = \frac{E_{pulse}}{\tau A} \tag{1.2}$$

For the interest of this work we will focus on ULDW in the contexts of semiconductors and more specifically of silicon. In the next chapter, the physical effects that contribute to the modification of the bulk are presented.

1.1 Propagation of light in silicon

The propagation of a laser pulse in a semiconductor can be described by the nonlinear Schrödinger equation [6]:

[1]For our purpose the intensity of a laser pulse is the optical power delivered per unit area. Its most common units are W/cm^2 (Watts per square centimeter)

$$\partial_z E = \frac{i}{2k_0}\nabla_\perp^2 E + \frac{ik_0 n_2}{n_0}|E|^2 E - \frac{1}{2}\sum_k \beta^{(K)}|E|^{2K-2}E - \frac{\sigma}{2}(1+i\omega_0\tau_c)NE \tag{1.3}$$

In the first term of equation 1.1 it is possible to recognize the Helmoltz equation solved for the paraxial approximation, which is valid under the assumption that the z-derivative of the amplitude function E is a slowly varying function of z:

$$\left|\frac{\partial^2 E}{\partial z^2}\right| \ll \left|k_0 \frac{\partial E}{\partial z}\right| \tag{1.4}$$

where k_0 is the wave number. The paraxial approximation is a good approximation for Gaussian beams, like transversely inhomogeneous laser fields. The second term in Equation 1.1, describes the Kerr effect, which contributes to the nonlinear self-focusing and self-modulation of the pulse. It is proportional to n_2, which is the non linear refractive index, and it contributes to increase the refractive index experienced by the pulse. The Kerr effect gives a positive shift to the refractive index that is proportional to the intensity of the electric field, or its square amplitude. The third term in Equation 1.1 takes into account the nonlinear multi-photon absorption, where $\beta^{(K)}$ is the coefficient for K-photon absorption. This is the key term that enables lasers with wavelengths that are typically transparent to be absorbed in the material. In fact, multi-photon absorption is not commonly favored in typical applications because its cross-section is usually negligible. Along the propagation, multi-photon absorption leads to the generation of free carriers to the detriment of the field amplitude. The generated free carriers shifts negatively the refractive index of the space volume they occupy, thus contributing to a self-defocusing of the pulse that is proportional to their density N. In the forth term of Equation 1.1 the diffraction of the field caused by the generated free carriers is taken into account. ω_0 is the central angular frequency of the pulse spectrum, while τ_c is the free-carrier momentum scattering time. Moreover, when free carriers are generated, they exist in a plasma phase, and they can absorb electromagnetic radiation via the inverse bremsstrahlung process. In the last term, σ is the inverse bremsstrahlung absorption coefficient.

Equation 1.1 is coupled with the time dependence of the free carrier density, that can

be described as follows [6]:

$$\partial_t N = \sum_K \frac{\beta^{(K)}|E|^{2K}}{K\hbar\omega_0} \tag{1.5}$$

With the same parameters mentioned as above. Other mechanisms do not play a role in the timescale of the pulse propagation, and free carrier recombination can be neglected because radiative recombination occurs on the nanosecond or even microsecond timescale [7], much longer than the pico- end even femtosecond pulses employed in the ULDW technique. The generation of free carriers is crucial because they transfer the energy of the laser pulse to the surrounding lattice. The density of the deposited pulse energy can be expressed as [6]:

$$\frac{\partial W}{\partial t} = \sum_K \beta^{(K)}|E|^{2K} + \sigma N|E|^2 \tag{1.6}$$

which takes into account the multi-photon and free carrier absorption. However, the pulse must be tightly focused to prevent the dispersion of the free carrier plasma. Due to the nonlinear nature of both absorption and self-focusing processes, it is not straightforward to predict at what pulse energy the pulse will collapse, particularly when considering the wavelength dependence of the participating processes [5].

To put light on the problem of sub-surface silicon processing the authors of [5] introduced a novel concept of nonlinear figure of merit (NFOM) that can be described as follows:

$$NFOM(I,\lambda) = \sum_K \frac{n_2(\lambda)}{\lambda\beta^{(K)}I^{(K-1)}} \tag{1.7}$$

with, λ the wavelength in vacuum, $n_2(\lambda)$ the wavelength-dependent nonlinear refractive index, I the field intensity, and $\beta^{(K)}$ is the coefficient for K-photon absorption.

To understand the complex interplay of involved nonlinear optical phenomena and the resulting beam propagation inside silicon, R. Richter has carried out numerical simulations solving the coupled Equations 1.1-1.1. Thus, the novel concept coupled the nonlinear absorption and self-focusing and made visible the prevalence of the Kerr effect over the K-th multiphoton absorption at specific rather narrow wavelength range around 2.1-2.2 μm. In Figure1.1 the NFOM calculated for silicon is presented. In the simulations only 2 and 3-photon absorption have been taken into account[8].

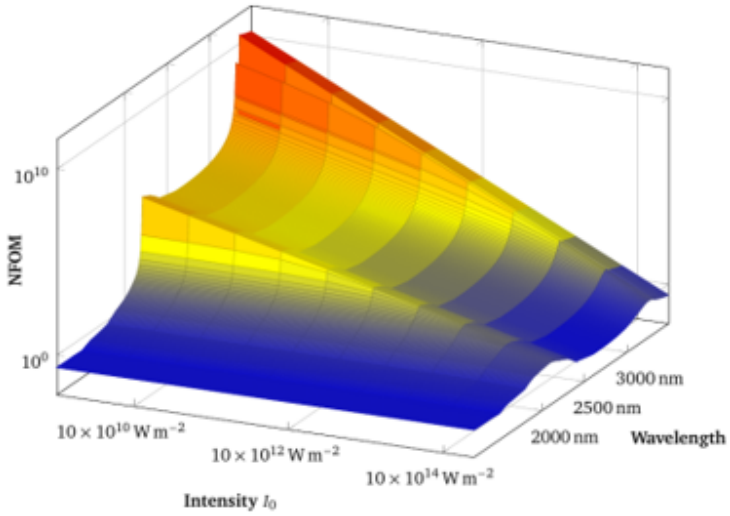

Figure 1.1: The NFOM as a function of the wavelength and the intensity of the laser pulse is shown[8].

2. Ultrafast Laser Direct Writing at NTNU

2.1 Setup

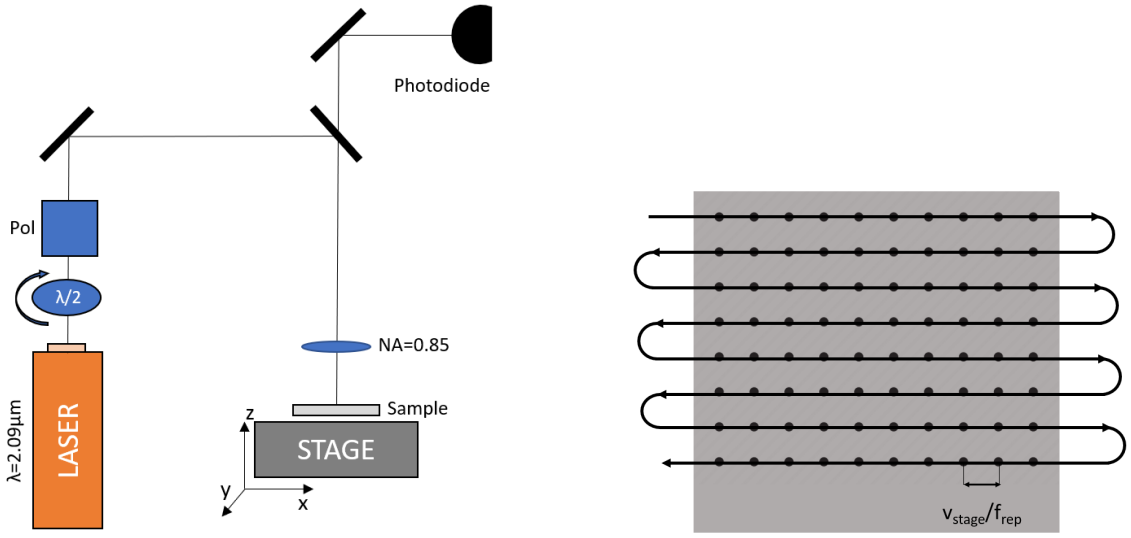

(a) (b)

Figure 2.1: (a) The setup at NTNU is made of a ”laser system”, in orange, and a ”delivery system”, all the remaining components.(b) Stage movement for the laser processing of the DUT (in gray). The separation between two subsequent modifications along the laser path is given by the ration of the stage velocity and the repetition rate of the laser.

We can consider the ULDW setup in the NTNU’s laboratories as composed of two parts: the laser system, and the delivery system. Ultrashort-pulsed mid-infrared laser from ATLA Lasers AS operating around 2.09 µm was used as a structuring tool, which we call here and afterwards “the laser system”. The ”laser system”is dedicated to the production of the pulsed beam at a wavelength of 2.09 µm, and pulse length of 2-5 ps. The ”delivery system” controls the average power of the beam with an attenuator (based on a half wave plate and a polarizer), focuses the beam with an objective (NA=0.85, with built-in aberration correction for silicon), and controls the movements of the sample with a moving

translation stage, ensuring excellent positioning speed, precision, and repeatability. The combination of high scanning speed and high laser pulse repetition rate ensured single-pulse laser processing - when every next laser pulse does not overlap with the region of silicon affected by the previous laser pulse. In combination with few-picosecond laser pulse duration, it allowed for minimized heat accumulation in the material affected by laser light and thus ensured ”cold” laser processing. To write laser modifications in the bulk of the device under test (DUT), the crystalline-silicon-based sample needs to have at least one highly polished side to allow a good penetration of the focused pulse without scattering due to roughness. However, two polished sides are preferred for inspection of the DUT after the processing by means of infrared microscopy. The DUT needs to be aligned perpendicular to the laser beam to obtain a uniform modification along the whole sample. Given a certain aberration correction value set on the objective, and working with low energy pulses, the sample is aligned by maximizing the reflection of the laser at four points on the DUT upper surface. The intensity of the reflected beam is measured using a photodetector and the sample is tilted and moved along the z axis until the maximum intensity is measured at all four points. The patterns that can be written by the setup are limited because the delivery system lacks a shutter to selectively block incoming laser pulses. In fact, the beam is composed by a continuous train of pulses at a rate f_{rep}. Moving the stage at a constant speed will implant defects at intervals of v_{stage}/f_{rep} along the path of the laser across the sample. In order to implant in an area, a meandering path can be traced across the DUT as shown in Figure 2.1b. While the laser is moved, for example, in x-direction, defects are implanted at regular intervals. Changes of the DUT position in y-direction are done away from the DUT to prevent an irregular spacing of defects. The defect implants can be constrained to a part of the DUT surface by applying a mask (usually a thin metal sheet with a cut-out) that is opaque to the infrared laser in areas where implants are not needed.

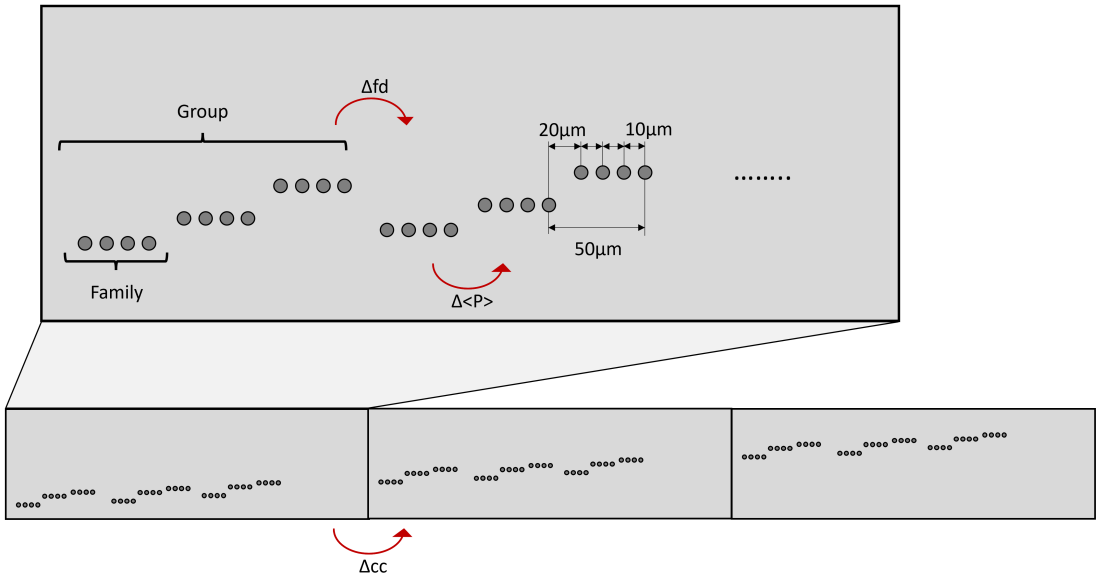

Figure 2.2: Standard scheme of laser processing to study the laser parameters, with cross section point of view. The modifications are organized in sections with different aberration correction, in which we find groups written at different focal depths. In the groups, the average power is the same within the same family of four single modifications.

2.2 Finding the writing parameters

At the focus point inside the silicon bulk many optical nonlinearities (2 and 3 photon absorption, Kerr effect, free carrier refractive index shift) contribute to the absorption of the optical energy into the lattice. All the applications of ULDW require to modify a certain material at a given depth z. Due to the complexity of the writing process, it is not trivial to know a priori which are the writing parameters that better suit the experiment. The optical nonlinearities are intimately related to the properties of the material under processing and to the depth we aim to modify. Hence, for every new material we must empirically find the laser parameters, and relate them to the depth at which we are obtaining the modifications. In fact, the standard procedure requires to experimentally scan all the possible combinations of the optical and laser parameters on a dummy sample of the material to process in order to measure the best fitting set for the desired application.

The optical and laser parameters we refer to are:

1. Average laser power: <P>. It is measured positioning a power metre after the attenuator in the delivery system. The modifications obtained with the setup at NTNU are produced by a single-pulse, so fixed the repetition rate of the laser, the average power is directly connected with the single pulse energy as E_{pulse}=<P>/f_{rep} (see chapter 1);

2. Focal depth: fd. The 0 µm focal depth is positioned at the top surface, and the movement of the stage of Δz corresponds to the same change in fd. Note that fd is not the position of the laser focus inside the material, which is instead determined by the refractive index felt by the laser propagating in the material;

3. Aberration correction collar setting "cc". The correction collar is a turnwheel on the objective lens that allows aberration correction for focusing light through the optically dense medium.

In Figure2.2 it is represented the standard writing scheme used to study the optical and laser parameters. The modifications are organized in *sections* with different correction collar setting, in which we find *groups* at different focal depths. In the groups, the average power is the same within the same *family* of 4 single modifications. The family made of 4 dots is like a fingerprint useful to better discriminate the laser modifications from other asperities on the cross section surface that can look similar under the microscope. Within the family, the center of the dots are at a distance of 10 µm while, the families are separated by 20 µm. This allows to further characterize the fingerprint of the modifications. It is important to point out that not always the modification is successful, and it happens to see families made of less then 4 dots.

2.3 Characterization of the modification depth

In this section we report the techniques used for the characterization of the resulting laser implantation. Infrared Microscopy (IRM), Optical Microscopy, and Scanning Electron Microscopy (SEM) are the mentioned techniques. The observation is done on the cross

section of the implanted specimen, that has to be polished with a grain smaller than 1 µm, i.e. less than the expected size of the laser modifications. Optical microscopy and SEM only require one polished cross section because they work in reflection, while IRM works in transmission, and thus require two polished sides parallel to one another. As a polishing tool we mostly used a optical fiber polishing machine. It works for small samples ($\sim 1 \times 1$ cm^2) that are think enough ($\geq$300 µm) to endure the mechanical stress. Thinner samples require to be encapsulated in resin before polishing to strengthen it and avoid fractures. The best contrast was achieved in the images obtained with IRM and SEM, that have shown interesting features reported in the next sections.

2.3.1 Optimization of the laser writing conditions

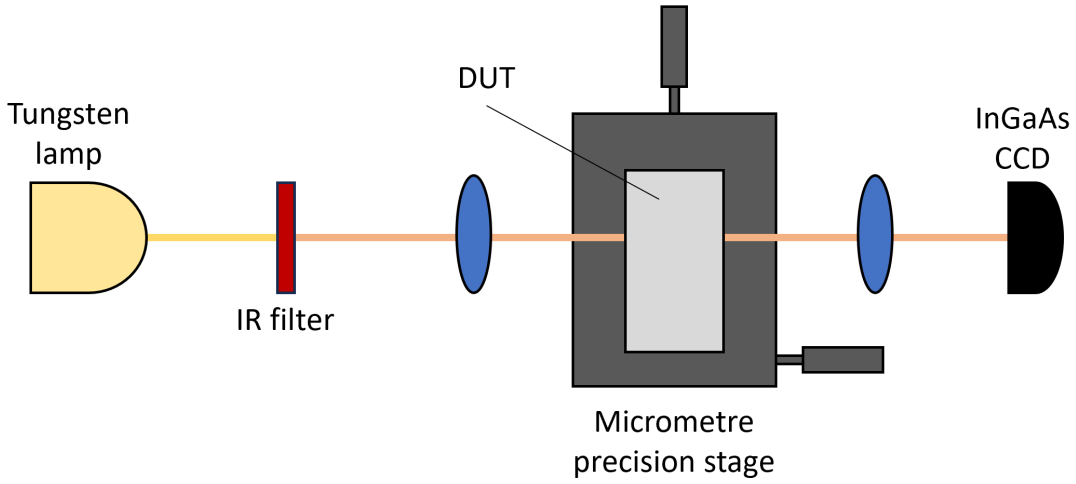

Figure 2.3: Setup of the homemade infrared microscope. An optical filter is used to select the infrared spectrum from a tungsten lamp. After passing through the device under test, the light is detected at the InGaAs CCD. A micrometre precision stage allows to scan the whole cross section of the sample under study.

After the implantation and the polishing procedure, the modified sample is ready to be imaged with IRM (Figure 2.3). In this configuration the laser-induced modification appears as a shadow spot due to the difference in refractive index between the modified material and the surrounding unmodified bulk (Figure 2.4), so it is possible to locate their

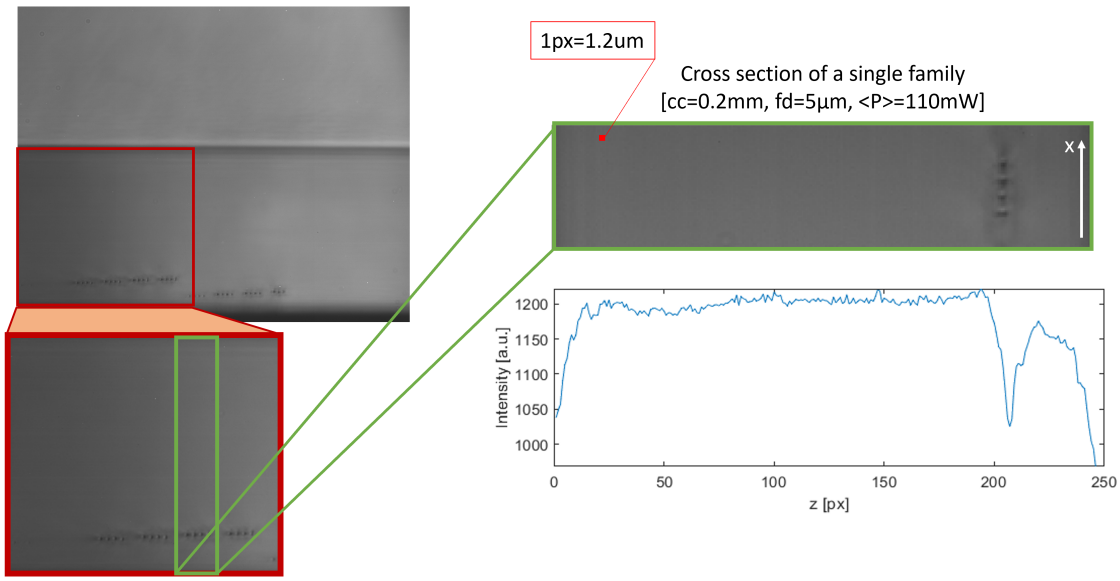

Figure 2.4: Top Left: IR image of a modified p-type (100) Si 300 µm thick sample. We can see two groups (fd=5µm and fd=0µm, in this case with the back surface as a reference) of modifications produced with cc=0.2mm, and families with <P>=[50,70,90,110,130]mW. The lowest <P> did not produce any modification. Bottom Left: the script allows to cut the IR image to select the single group within the sample. Top Right: a further selection isolates the single family produced with [cc=0.2mm, fd=5µm, <P>=110mW]. Bottom Right: Averaging the pixel intensity in the x direction it is possible to individuate deep in correspondence of the family position.

implantation depth given as the distance from the top or bottom surface depending on the most convenient description. Given a well organized implantation scheme (Figure2.2), and a well aligned sample, the imaging is done smoothly. In fact, we know the size of a family and how many are present in a group, from which we get an overall size of the group Δl. Now, if we position the sample such that on camera the first family is positioned at the edge, from there on we can just blindly move the stage of a distance Δl and take pictures of the groups one after the other (Figure 2.4). At this point, if the application requires to find one or two sets of laser parameter, the process to find the parameters can be relatively fast.

It might be useful, though, to characterize a wide range of depths and get a good char-

acterization of the relation z = z(<P>, fd, cc). For this reason it can be shown as a proof of concept that the imaging process can be automatized. In fact, with the use of a programmable moving stage the images can be taken automatically, substituting the manual steps of moving the stage and saving the images. Subsequently, as presented in Figure 2.4, the images can be processed to select the cross section of one group, and by dividing in equal parts, we are left with the cross section of one family. The images are saved as a 2D matrix, with each element corresponding to the intensity recorded by one pixel of the CCD. In this proof of concept, to discriminate the boundaries of the imaged sample, i.e. the top surface and the bottom surface, an average along the x direction allowed to distinguish three regions with different contrasts, hence different average intensities. The boundaries among the regions corresponds to the edges of the sample. The same idea was implemented to find the z position of the family for their cross section. In Figure 2.4 the average along x of one family IR image is plotted in a graph where a deep is present in correspondence of the selected family.

The calibration method used in this brief analysis relied on the sample width, with known value of $300(25)$ µm, giving a resolution over 1µm/px. However, the discrimination of the sample edges is not quite clear, the reason laying probably in the sample not being perfectly in line with the optical path of the light. As a consequence, the absolute depth is hard to determine with this microscope. However, in an application that do not require the implantation to be done in specific absolute positions, but instead can be done in general portions of the sample, it is still possible to reach quite a good accuracy in the relative positions of the modifications. Adding up to the limits in resolving the edges of the sample, there is the uncertainty of the sample thickness itself. A better calibration procedure can be implemented producing two modifications at a certain distance, well known thanks to the moving stage, and use them as a reference for the calibration. To further improve the measurements the background noise of the CCD can be measured and removed, and a Gaussian fit can be performed on the deep in intensity given by the presence of the modifications. In case it is required to modify the sample next to the surface, this imaging method can still be used to get an idea of the laser parameters that write next to the surface, but it is evident that a different technique is required. In the next section scanning electron

microscopy is used to overcome this limitation.

2.3.2 Single Vs Multiple pulses

Single pulse modification

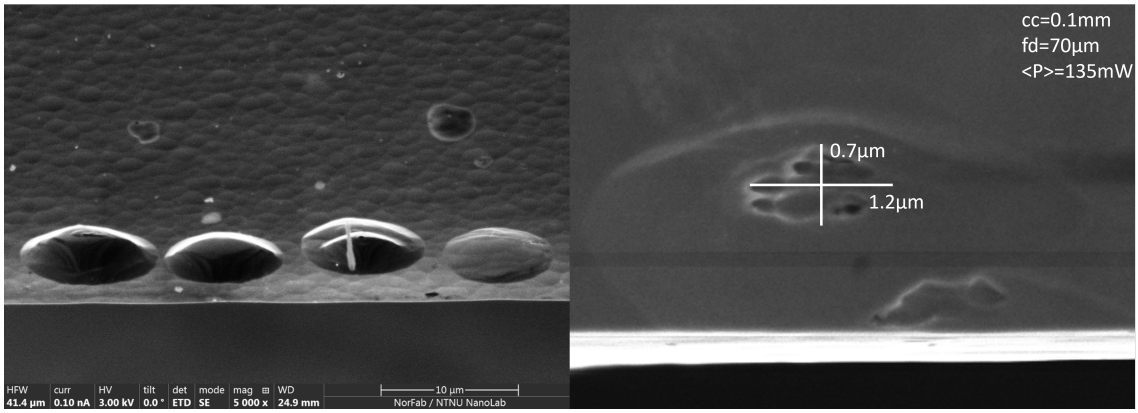

Figure 2.5: Representative SEM pictures of etched samples of p-type Silicon. Left: 45° view of a family of etched modifications. The funnel like structure of the etched hole is visible. The surrounding surface was subjected to the Sopori etching and it resulted in a fish-skin-like texture. Right: zoom top view of an etched single pulse modification made with laser parameters [<P>=135 mW, fd =70 µm, cc=0.1 mm].

Scanning electron microscopy (SEM) comes to mind when in need of a high resolution imaging technique. It is reported [4], that large volumes of laser-induced modifications in crystalline silicon are visible under SEM after mechanical polishing because of cracks forming in the volumes during the polishing that become visible with SEM. However, single pulse modifications[1] did not become visible. The modifications produced with the ULDW setup at NTNU are expected to be spheres of $\sim$1 µm in diameter [2], and thus require an etching step to allow their imaging with SEM, although it is a destructive procedure. It is then important to etch the modified area with a chemical that selectively etches

[1]Note that in this case by "single pulse modification" we mean modifications produced in a line along x (or y) with step in x (or y) of 1 µm. Each of the pulses in the sequence can be considered a single isolated pulse as they do not seem to be affected by refractive index changes produced by the previously written pulse.

the modified volume and leaves completely or almost unaltered the surrounding volume. Due to the group experience with this solution, we used Sopori[9], an HF-based etchant. The employed recipe is described in AppendixC. In Figure 2.5 we report representative SEM pictures of p-type Si wafers processed with ULDW and etched with Sopori. Some peculiar features are visible, and can suggest the limitations of the followed procedure. First of all, SEM definitely allows to reach a finer resolution in the characterization of the laser modifications. The position of the modifications compared to the edges of the sample is well resolved, and it is possible from SEM analysis to assign a better value of obtained depth to a given set of parameters. However, the etching procedure requires the whole sample to be dipped in the Sopori solution. Thus, the technique is destructive and modifies the original sample, not only etching the laser modifications, but also the surrounding volume. It is visible from Figure 2.5 how the surface presents a fish skin texture suggesting that Sopori is also etching crystalline silicon. As better reported in 4.2, the etching rate of the Sopori acting on the silicon bulk was estimated to be $0.22(3)\,\mu\mathrm{m\,s^{-1}}$ (underestimated[2]). 25 s of exposure to Sopori lead to the etching of over 5 µm of silicon, and other etching solutions, less corrosive, should be preferred. As an example, Write etch[9] can be a less aggressive alternative. Nevertheless, the effects of Sopori on the laser modifications are quite interesting, as they reveal a hollow funnel-like structure. This shape may be the consequence of an inner core of the modification being denser in lattice defects, mimicking the Gaussian profile of the energy of the laser pulse. However, different average powers of the pulses do not result in different sizes of the etched modifications, which instead appear all quite similar in size. The reason may lay instead in the stresses generated by very small modified volume in the center of the modification, which results in an more easily etched volume. The average size of an etched modification is quite hard to define since the edges are irregular, but as a general value we find 5 µm for the horizontal length and 3 µm for the vertical length. This asymmetry may be due to the

[2]The white halo that is visible at the Si-air interface (Figure 2.5) brings uncertainties on the position of the sample surface. The brightness on this area is due to the secondary emission of electrons from the bottom side of the silicon sample, and cannot be avoided. The bottom of the sample is thus considered above the bright area.

pulse shape at the focal spot.

Multiple pulse modifications

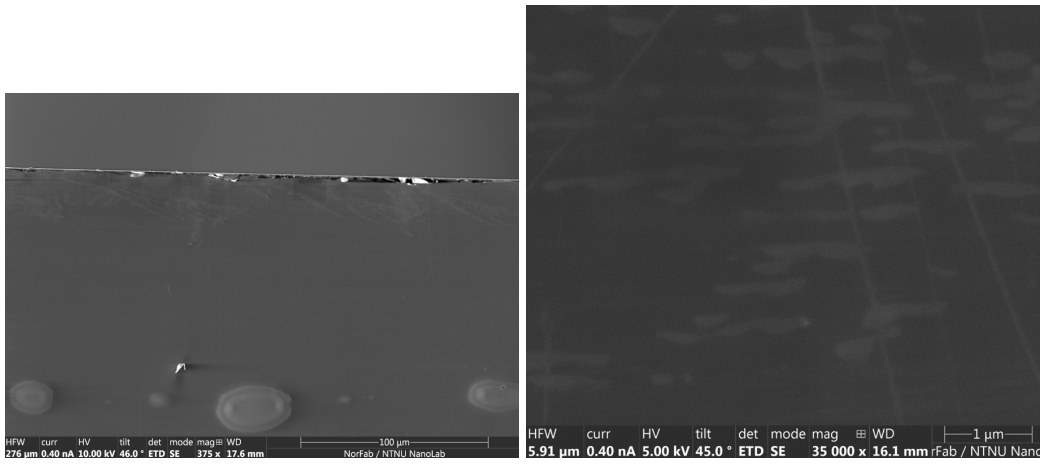

(a) (b)

Figure 2.6: (a) We report a SEM image of the cross section of sample S1 grid 1×1 µm^2. Multiple layers of laser modifications are visible at different depths. (b) A focus on the cluster of multiple laser-induced modifications.

While single isolated modifications were not resolved with SEM without the Sopori step, densely implanted samples present visible features under SEM (Figure 2.6). Different implantation densities have been explored by implanting different grid patterns in a p-Si (100) 0.17-0.23 cm sample, with steps from 1 µm to 6 µm (see Section 4.2). The laser parameters have been kept constant during the implantation and for the different grids in order to aim at $\sim$5 µm of depth. After the implantation, one side was lapped to expose the cross section and observe the implantation depth. The results show that in grids from 3×3 µm^2 and over, the modifications are not visible with SEM. While in grids up to 2×2 µm^2, a collective behaviour can arise. The modified volume becomes thicker and wider, and its depth drifts towards the laser source even though the laser parameters have been kept constant. Tokel et al. [4] have reported that a when sequence of pulses is implanted with the same laser parameters and focusing at the same depth, the formed structure is not a wider sphere. Instead, the n-th pulse modifies the refractive index of the silicon

crystal producing a convergent lens-like volume. As a consequence, the (n+1)-th pulse is subjected to a convergent lens effect, that makes the pulse collapse right after the n-th modification, i.e. induces a modification at a different depth. In Tokel et al. the setup was such that the (n+1)-th pulse was implanted further from the source. In our setup, since we wanted to produce a grid, we did not implant at the same xy position, but only at the same depth z. Thus, the effect of the change in refractive index arises only for dense enough patterns, such that the (n+1)-th pulse is near enough (in the xy plane) to the volume modified by the n-th pulse. It is not yet well understood how and in which phase the structure develops under influence of laser light. This is currently under investigation in frames of the "MIR" project. In fact, different structures arise from dense grids, albeit they all share some common features.

- The modified volume is thin ($\sim$1µm) near the surface and it thickens ($\sim$5µm) while developing towards the bulk.

- The modifications can be present at the same time in two different z positions. Mostly, in the bulk and at the surface.

- In the areas where the modifications are near the surface, the surface itself presents a grating-like pattern with crests with distances $\sim$100 nm. While, in the areas where the modifications were implanted deep enough ($>$ 5 µm), the surface presents less prominent damages, although still present (see Section 2.3.3).

- Even though the laser parameters (calibrated for single isolated pulses) were used to obtain modifications at $\sim$5 µm of depth, the development of the structures was seen to extend from 0 to 20 µm of depth.

- For certain values of laser parameters, a structure of constant thickness ($\sim$5 µm) can be inscribed with constant depth ($\sim$20 µm) for a long distance ($>$100 µm).

- The same structures are reproducible on the same substrate by using the same writing parameters.

2.3.3 Spurious surface damages

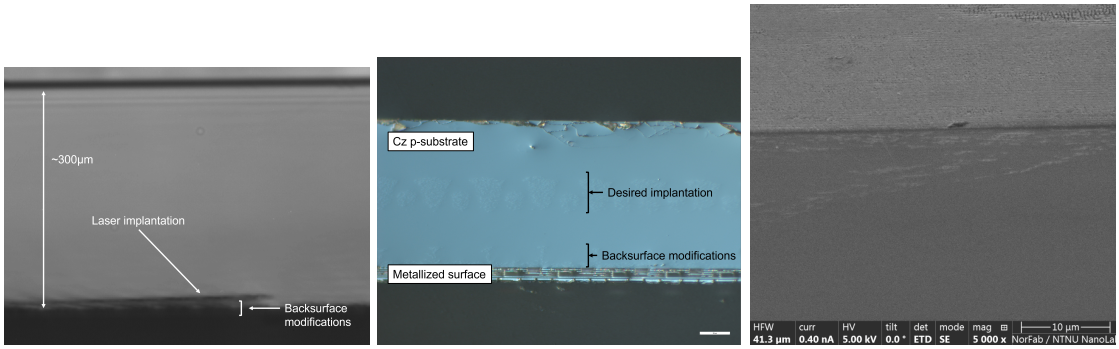

(a) (b) (c)

Figure 2.7: (a) IR image of the cross section of a laser implanted (100) p-type Si sample. At the bottom, the laser-implanted structure is visible as a shadow, under which other shadows are present at the back surface. The shadows on the back surface may be modifications produced by the leftover pulse energy, not completely absorbed at the level of the laser-implanted structure. (b) Optical microscopy image of the cross section of a laser-implanted MALTA2. Undesired modifications next to the metallic layer are evident. [Figure from private communication with Mickaël Denis Crouvizier, taken with Axio Imager.Z2 microscope, Axiocam 506 detector, and EC Epiplan-Neufluar 50x/0.8 HD DIC objective] (c) SEM image of the cross section of sample S2 1×1 µm^2 grid. Laser modifications are visible both in the bulk and near the surface at different depths.

When the pulse is not completely absorbed at the focal spot, the back reflection of the first part of the pulse can overlap with the forward moving part of the pulse thus generating a second focusing with subsequent modification of the material (see Figure 2.7). Moreover, modifications of the back surface are easier to obtain because they require less absorbed power than modifications inside the bulk. Evidence of multiple modifications are observed in most of the implanted samples and the effect is even worse is the specimen presents a metallic layer at the back, as it is for MALTA2 (Figure 2.7b). Even for implantations that happen deep in the bulk, the surface can still be modified by the remaining pulse energy. Different implantation densities have been explored by implanting different grid patterns in a p-Si (100) 0.17-0.21 cm sample, with steps from 1 µm to 6µm.

The laser parameters have been kept constant during the implantation and for the different grids in order to aim at $\sim$5 µm of depth. The surface modifications are always present although diminishing in affected area and dimension of the damage for the different samples. The damages present a grating-like structure with periodic crests. The laser system at NTNU produces a pulse of 4 ps of 1200 µm in the air. Assuming a refractive index around n_{Si}=3.46987, the length of the pulse in in silicon can be estimated to be around 346 µm. This is long enough to allow an overlap of the incoming and back reflected part of a pulse. The reflection is particularly strong on metal layers, where the non-absorbed part of the pulse is back reflected completely. This is not the case for samples that have a polished silicon surface. Here, back reflection occurs because there is an air gap between the back surface of the device under test (DUT) and the holder of the stage on which it sits. The reflection coefficient for a beam normal to the DUT is the following

$$r_p(\Theta_i = 0) = r_s(\Theta_i = 0) = \frac{n_i - n_t}{n_i + n_t}$$

Where p and s are the polarization components, Θ_i is the angle of incidence of the light, n_i and n_t are respectively the refractive index of the material in which the light is incident and transmitted. The fraction of reflected power is then simply stated by the reflectance

$$R = |r|^2$$

At high beam intensity, the refractive index of the material changes due to optical non linearities (see chapter 1.1). As a consequence, it is hard to estimate the refractive index of silicon when the pulse arrives at the Si-air interface, but we can still have an insight on the order of magnitude of the reflected power by working with low intensity. For wavelength of 2.09 µm, we have n_{air}=1.000273[10], n_{Si}=3.46987[11], and a reflection coefficient of r_{Si-air}=0.5525. So, the reflected power accounts for R_{Si-air}=30.52% of the incident power. To reduce this effect, a solution might be to use a drop of liquid as a contact between the sample and the holder. The higher refractive index will reduce the reflection; in fact, already for water (n_{H_2O} = 1.3015) the reflected power is R_{Si-H_2O} = 20.65%, a reduction of 32.33% compared to air. Since, the reduction of the reflected power is a common problem in optical applications, many index matching liquids are commercially

available. As an example, Cargille provides a BK 7 glass matching liquid with refractive index n_{BK7} = 1.4931, which gives R_{Si-BK7} = 15.86% which allows for 51.96% reduction of back reflection compared to air.

3. A target for the Bose-Einstein condensation of positronium

The goal of this chapter is to present the motivations that led to the attempt to produce the positronium target, and to explain the design choices taken to produce it.

3.1 What is positronium?

Positronium (Ps) is the result of the bounding between an electron (e^-) and its antiparticle, the positron (e^+). This makes it the lightest known bound state within two particles, with a mass of $m_{Ps} \approx 1.022$ MeV given by the masses of e^- and e^+ of 511 keV minus the binding energy, equal to -6.8 eV for the lowest energy level. Some of the qualities of positronium that make it attractive to fundamental physics research are the following:

- Ps is a pure leptonic hydrogenoid atom kept together by only electromagnetic interaction;
- It has a mass lower than any stable atom;
- Ps in the ground state energy exists in two different spin configurations: the singlet state with spin 1, called para-Ps (p-Ps), and the triplet state with spin 0, called ortho-Ps (o-Ps);
- Ps is an unstable atom that decays spontaneously in a vacuum: p-Ps decays into two photons with lifetime of 125 ps, while o-Ps decays into three photons with lifetime of 142 ns.

3.1.1 Positronium formation

Positronium can be efficiently produced in certain solids via positron implantation. When a positron beam of few keV is implanted in matter, several processes can occur, and among

them the e^+ can bond with an e^- of the medium forming Ps. The bonding can happen in the bulk or on the surface; however, the formation in the bulk is allowed only in insulators, because in metals and semiconductors the high electron density screens the positron-electron interaction destroying the Ps binding [12]. While due to the already short lifetime p-Ps can be only marginally affected, the o-Ps can decay by pick-off annihilation (i.e. annihilation with an electron of the material) into two gammas with a reduced lifetime down to few nanoseconds. Ps formation is permitted on the surface of metals and semiconductors by the presence of e^+ traps where the electronic density is lower [12]. The formed Ps can escape by thermal detrapping, and for the emission to occur the Ps formation potential must be negative

$$\varepsilon_{Ps} = \Phi_{e+} + \Phi_{e-} - 6.8eV < 0 \tag{3.1}$$

where Φ are the work function of e^+ and e^-.

3.1.2 Positronium formation and cooling in nanochanneled silicon

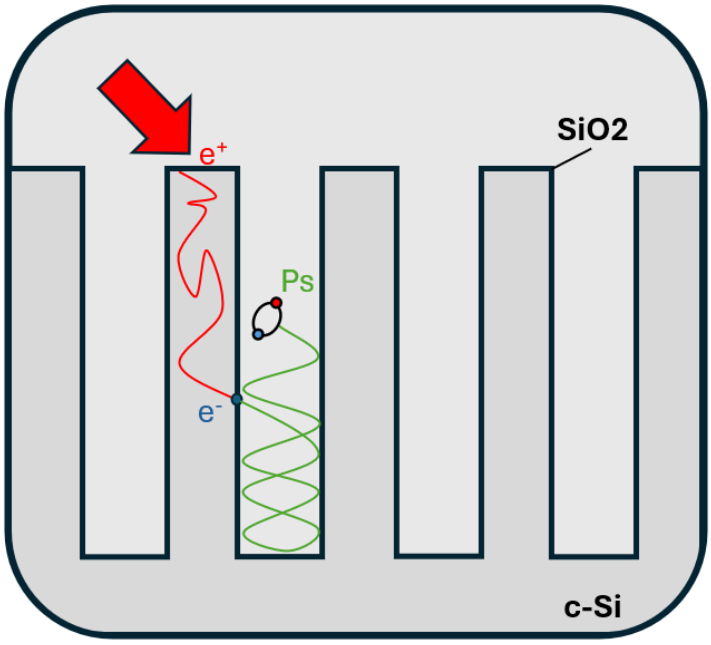

Figure 3.1: Ps formation in nanochanneled silicon.

The cooling process of Ps[1] is fundamental for a plethora of experiments where the requirement of cool Ps is key. A nanochanneled silicon target is the perfect tool both to produce and directly cool Ps efficiently. It consists in a comb of channels with a diameter of few nanometre grown on a silicon crystal. Thanks to the high surface to volume ratio, nanochanneled silicon covered by few nanometres of SiO_2 shows high (54%) e^+-Ps conversion efficiency [13].

Ps in a nanochannel behaves like a quantum particle in a well. Its wave function overlaps with the phonon states of the lattice structure of silicon [14]. With the generation of phonons to the detriment of the Ps energy, the Ps cools down with a consequent thermalization with the lattice, i.e. with the nanochanneled silicon target [15]. With only one way out, a Ps beam is emitted from the nanochanneled silicon target, readily available to be used in other experiments. As an example, a nanochanneled silicon target at the AEgIS collaboration at CERN is used to convert a positron beam into a Ps beam, that is employed in direct tests on antigravity or the production of antihydrogen [16], or for the spectroscopic analysis of the Ps atom itself [17]. In all these experiments, the cooling process of Ps is fundamental to improve the precision of the experiments. It increases the cross section of exchange reactions for antihydrogen production [18] and it sharpens the spectroscopic measurements of Ps [19]. The thermalization time is fundamental because the lifetime of Ps in a vacuum is 142 ns, but it is reduced in a confined environment [12]. Wide nanochannels allow to reach relatively low temperatures, albeit at the expense of a longer cooling time [14]. The length of the nanochannels, however, must be taken into account too because Ps needs to travel the nanochannel length to result in an out coming Ps beam for experiments to follow. Therefore, different applications require the correct balance of the nanochannels' diameter and length.

3.1.3 Positronium Bose-Einstein condensate

The production of the first positronium Bose-Einstein Condensate (Ps-BEC) had been envisioned since 1994 [20]. The observation of a BEC made by purely leptonic atoms that

[1]From now on, if not specified otherwise, with Ps we will refer to o-Ps, as the short lifetime of p-Ps makes it impractical for use in most experiments.

are their own antiparticle make Ps-BEC an extremely intriguing physical creature.

In the case of Ps the phase space density required to undergo a phase transition into a BEC is:

$$n = \frac{2.612}{\lambda_{DB}^3} \tag{3.2}$$

$$\lambda_{DB} = \frac{h}{\sqrt{2\pi m k_B T}} \tag{3.3}$$

Where λ_{DB}, m and T respectively are the De Broglie wavelength, rest mass and temperature of the Ps atom. At a few tenth of Kelvin the required phase space density is $\sim 10^{15}$ Ps atoms/cm^3, while at milli Kelvin it is $\sim 10^{12}$ Ps atoms/cm^3 [21]. Therefore, there is an interplay between the phase density and temperature of the Ps gas. The maximization of the Ps' phase space density and the minimization of its temperature are to be pushed to the limits for the experimental success of Ps-BEC.

In order to achieve Ps-BEC, experimental requirements have been advanced both on the design choices of the experiment and the techniques for the cooling process. Some designs for such an experiment have been based on the idea of depositing a large number of Ps atoms inside a cavity formed within a porous insulating material like silica (SiO_2). A problem is that the cooling time of the Ps is proportional to the effective mass of the atoms in the cavity walls times the mean free path of the Ps in the cavity, and it would be difficult to obtain a below room temperature gas in a 100 nm diameter cavity within one mean lifetime without laser cooling . Moreover, Ps atoms inside such a cavity will likely become stuck to the inner walls of the cavity at room temperature and therefore might not be able to form a Boltzmann gas, let alone a BEC, in the vacuum space of the cavity[22]. Recently, Asaro et al. proposed a target design consisting of a cavity 100 nm tall and 1 μm wide obtained by gluing a flat diamond surface on a flat porous silica surface. The cavity may be formed by milling down a groove with the dimensions of the desired cavity before bonding the two surfaces. Porous silica would act as an e^+-Ps converter from which Ps can enter the cavity. Eventually, with a high enough yield (n $> 10^{19}$Ps/cm^3) the surface of the cavity would be filled with trapped Ps, and the exceeding Ps could escape into the cavity void and form a BEC with a critical temperature of about 170 K [22].

3.2 Cooling of positronium

In a recently published paper, Glöggler et al. [23] of the AEgIS collaboration, and in a simultaneous paper uploaded on arXiv by Shu et al. [24], two different methods have been presented to laser cool Positronium. As mentioned already, positronium has an hydrogenoid structure, and thus do its electronic levels. Glöggler et al. have exploited the 1^3S-2^3P transition to laser cool positronium with a broadband laser pulse centered at 243 nm. The pulse reduced the temperature of the positronium cloud of a total of 210 K, starting from a mean temperature of 380 K. In the laser cooling process, the only limit to the cooling of the gas is given by the recoil limit. If a laser pulse at 243 nm is used such a limit corresponds to 0.6 K. Mariazzi et al. [15] have demonstrated that a significant fraction of positronium (9%) can be produced in thermalization with a nanochanneled target kept at cryogenic temperatures of 150 K. Thus, the same laser cooling process can be applied to a positronium gas already in thermalization with the target achieving below Kelvin temperatures. This possibility, combined with possibility to accumulate $\sim 4 \cdot 10^9$ e^+ in the AEgIS beam line [25][26] and their compression in a bunch of diameter $\sim$0.5 mm, can unlock the density and temperature required for the production of the first positronium Bose-Einstein condensate. Another requirement for the laser cooling to occur is a high enough density of photons at 243 nm inside the cavity. In the UV spectrum, silicon presents a metal-like behaviour, with a penetration depth[2] of $\sim$600 nm [27]. Thus, it becomes even more fundamental to obtain the cavity at a depth ≤ 1 μm. With a strong enough laser pulse the fraction of photons reaching the cavity can be significantly enough; moreover, the nanochanneled feature required for the conversion is expected to reduce the absorption of the material.

3.3 The target

Within the collaboration between the University of Trento and the Norwegian University of Science and Technology (the Antimatter Group at UNITN and the Laser Group at NTNU) a target for future Ps-BEC tests is under study (Figure 3.2). The target should

[2]Penetration depth: when the light intensity has fallen to 36% (1/e) of its original value.

come from a single piece of silicon crystal, with a buried cavity some hundreds of nanometres tall, and some micrometres wide connected to the surface by a comb of nanochannels. Ps atoms produced in the nanochannels will diffuse along them loosing a fraction of energy and will be finally confined in the cavity. Moreover, the nanochannels can be further grown under the cavities to unlock a wider volume of conversion. In fact, the implantation distribution of positrons in the target has to be taken into consideration. The Makhovian profile is a popularly used formula to describe positron implantation profiles of slow positron beams [28]. The distribution presents a wide peak with a prominent tail at high depth values. Thus, it is possible to tune the energy of implantation to center the Makhovian distribution in the nanochannels over the cavity, and exploit the nanochannels present under the cavity to target the fraction of positrons implanted with higher energies. Being captured inside the walls of the nanochannels, the positronium should fall in the cavity nevertheless, increasing the overall conversion efficiency of the target. A few nanometres of TiO_2 can be grown on top of the nanochannels in order to further contain the positronium inside the target.

The design of such a target presents some differences compared to the target presented by Asaro et al.: a different e^+ to Ps medium converter is used (nanochannels instead of porous silicon); the conversion medium is present on top and under the cavity; a TiO_2 cap to avoid Ps emission outside the target; the target comes in a single solid piece; the cavity is expected to be produced in series on a surface of $\sim$1cm^2 over a silicon wafer.

The synthesis of such a target can be achievable by exploiting the sub wavelength precision of the ULDW setup at NTNU to modify the resistivity of the silicon substrate on which the nanochannels will be grown. In the next chapter our experimental approach will be presented showing its achievements and limitations, as well as the suggested improvements to be explored in future studies.

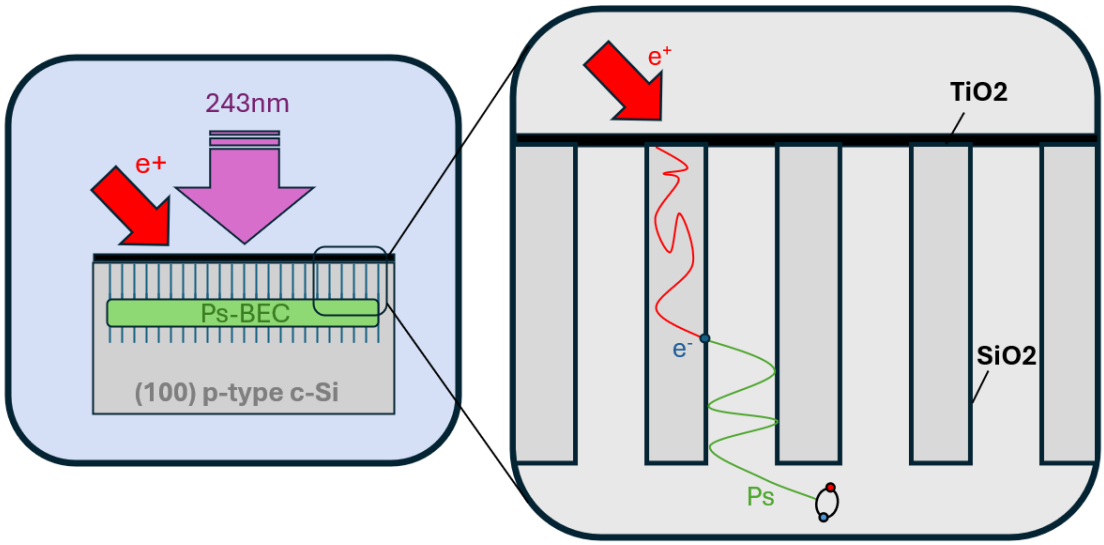

Figure 3.2: Envisioned target for the production of a positronium Bose-Einstein condensate.

4. Positronium target: Experiment

In this chapter we report the experimental approach taken to produce the positronium target, and the characterization done after each step of the production.

4.1 Experimental approach

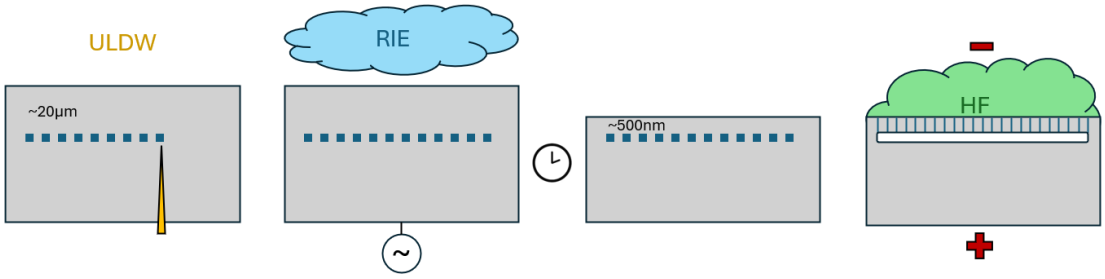

Figure 4.1: The stages of the target production are reported. Left: A group of laser induced modifications is written in the p-type (100) Si sample some micrometres from the surface. Center: Reactive Ion Etching is used to thin the bulk volume over the modified volume. Right: nanochannels are grown with electrochemical etching in an HF solution.

The idea behind the experimental approach we took for the production of a positronium target was the possibility to modify the resistivity of the sample locally by exploiting the precision of ULDW. The resistivity of the modified volume is expected to be higher than bare bulk due to lattice defects and stresses introduced with the laser. Resistivity measurements of the modifications produced with ULDW are not common in literature as the main features that are usually exploited are optics related. However, even though the physics is quite different, we can use as a reference the resistivity changes produced by irradiation damage in silicon detectors to understand what may happen with ULDW. The damage of high doses of radiation corresponds to atomic displacements in the lattice, and as reported by Pirollo and Li [29] [30], the radiation-induced damage in the electrically neutral bulk of silicon detectors (where a sensor is not fully depleted) induces deep levels

that can cause carrier removal, leading to a dramatic increase in bulk resistivity with a saturation at a value close to the intrinsic resistivity. Hence, it is reasonable to think that if the laser-induced modifications produce a similar effect as for the radiation damage to the Si lattice, then a local increase of resistivity can be achieved with ULDW. To be mentioned is our attempt to measure the change in resistivity of the ULDW modified volume with a 4 point probe reported in AppendixB, that was not successful to distinguish the contribution of the modifications due to the small volume to be measured. The need of a higher resistivity in the modified volume will be clearly evident. As we have already explained (see Section3.1.2), on the surface the targets need nanochannels to allow the conversion of the e^+into Ps via the extraction of an e^- at the SiO_2-air interface. The growth of the nanochannels is achieved by means of electrochemical etching (ECE), where an etching solution is employed under an electric field to guide the ions of the solution along the direction of the field. The diameter of the produced nanochannels is sensitive to change in resistivity of the material, the higher the resistivity the bigger the channels [31]. Thus, if the nanochannels are grown in a substrate that presents a gradient in the resistivity, it is reasonable to expect that a corresponding gradient in the diameter of the nanochannels can be found as well. When reaching the modified volume, the nanochannels should grow big enough in diameter so to merge and form an open volume (see Figure4.1). A subsurface open volume connected to the surface by means of nanochannels makes the perfect Ps target, at least from a topological point of view. In fact, although the topology is correct, it is difficult to obtain the correct sizes of the cavity and nanochannels to optimize the fraction of Ps emitted with an energy at thermal equilibrium with the medium [14]. Ideally, the resistivity profile should resemble a step function to get a clean edge where the nanochannels can merge together. SEM pictures of densely written targets show a domain of the modified volume well distinguishable from the matrix. However, it is also evident that the modifications are not commonly merged, rather isolated by few hundreds of nanometers of silicon matrix.

4.2 Laser processing

Batch n°1

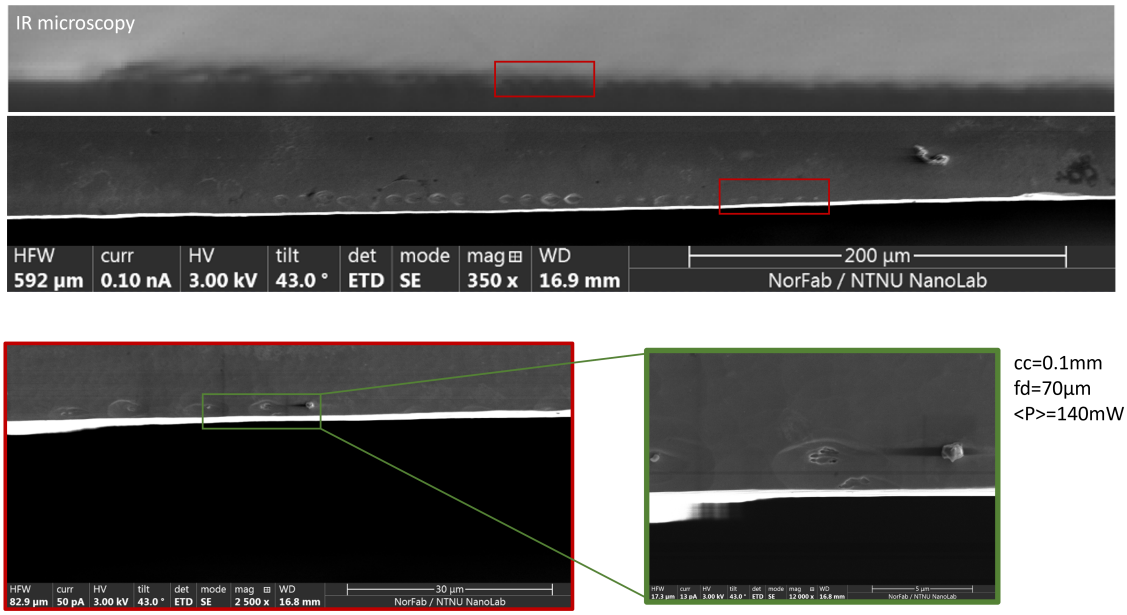

Figure 4.2: Sample from a p-type (100) 0.17-13 Ω cm wafer, is presented after ULDW for both, and after Sopori etching for SEM images. Top: two pictures (IR at the top, SEM at the bottom) of the same group of modifications are reported for comparison. The dots have been written with cc=0.1 mm, fd=70 µm (top surface as reference), and <P> = [180, 170, 160, 150, 140, 130, 120, 110, 100, 90]mW ordered as they appear in the pictures from left to right. Bottom left: zoom on the family at <P>=140mW. On its right, the family at 130mW was etched half way through. Bottom right: zoom on a single dot modification etched with Sopori.

The substrate material selected to produce the positronium target is crystalline silicon p-type , with resistivity 0.17-0.23 Ω cm, and (100) orientation. This material presents the right values of resistivity to grow nanochannels with diameter of 5 to 10 nm [13]. The processed samples come from a wafer 300 µm thick. Before processing, the first step consists in finding the best laser parameters to induce modifications next to the surface. Focusing the laser just under the interface where the laser enters in the material is quite

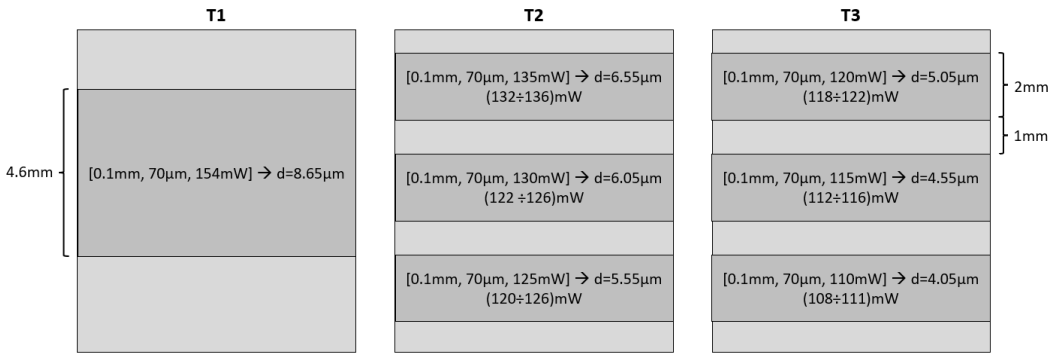

Figure 4.3: The writing scheme of the samples T1, T2, and T3 are shown. All have been processed with a grid of modification with step of 1 µm in both x and y directions. The ranges reported for the average power are due to laser instability and have been recorded before and after the processing.

challenging, and it results easier to process the sample next to the bottom surface of the sample. Following the steps presented in chapter2.2 we selected the best laser parameters for our purpose. At first the sample was polished and studied with IR microscopy to identify the regions of interest, and select the most interesting parameters to be imaged with SEM. Subsequently, in the ISO7 cleanroom at the NanoLab of Sintef, the sample was etched with Sopori, and studied with the FEI SEM Apreo.

In Figure 4.2 some IR and SEM images of a group of promising parameters are reported. The dots have been written with cc=0.1 mm, fd=70 µm (top surface as reference), and <P> = [180, 170, 160, 150, 140, 130, 120, 110, 100, 90]mW ordered as they appear in the pictures from left to right. Even though there was no change in the focusing depth, the higher the average power, the higher the modification families are located due to the focusing effect of the Kerr non-linearity. In this specific area next to the Si-air interface with cc=0.1 mm, and fd=70 µm, it appears from the measurements that the average power of the laser affects the modification depth with a rate of $\Delta_{<P>} \approx 0.11(1)\ \frac{\mu m}{mW}$. This value depends on the relative depth among the modifications, so any uncertainty on the position of the Si-air interface is avoided.

In the picture (see Figure 4.2) one family of 4 dots is framed in red in both IR and SEM images. From a direct comparison of the two images it appears that the families with

lower power have been washed away after the etching step with Sopori. In the bottom left picture it is also visible another family at the right, that is etched half way through. The surface have been etched partially removing the modification the nearest to the surface. Assuming that all the 5 families that have been removed after the etching have been written in bulk, and the last family was exactly at the surface, we can use the rate $\Delta_{<P>}$ to estimate the etching rate of Sopori on unmodified silicon. The average power spanned by the 5 families is $50(1)$ mW, that corresponds to $5.5(6)$ µm of silicon etched by Sopori in around $25(1)$ s of etching time[1], giving an etching rate of $0.22(3)\,\mu m\,s^{-1}$. This value seems reasonable, compared to the etching rate reported in [9] of around $0.33\,\mu m\,s^{-1}$ that is referred to a Sopori solution HF:CH_3COOH:HNO_3 with molarity 36:20:2 while ours was 36:15:2. Hence, it is convincing that the etching step is destructive, and the need of another non destructive technique would come in hand for precision measurements in the future. Or instead, other less aggressive etching solutions can be used, Write-etch as an example [9]. Nevertheless, the process allowed us to better identify some set of parameters to attempt a laser processing for the production of targets for positronium experiments. In Figure4.3 we report the writing scheme and the set of parameters used with the corresponding expected depth referred to the centre of the modification. From SEM pictures it is hard to assess the diameter of the modifications, since they are taken after Sopori etching, but indicatively it appears to be in the range [0.6÷2]µm. With the subtraction of half the diameter from the reported modifications' depths, we get an idea of the depth at which the resistivity should change. The decision to use these values of average power was done aiming to center the modifications at few micrometres from the surface, taking into account the possibility that the electrochemical etching required to grow the nanochannels could thin the gap with the surface. Moreover, we should recall the decrease of output laser power in time coming from the non-perfect stability of the laser setup when operating for long times (hours). The decrease of output power is not taken into account when reporting the values of the laser's average power, which suggests that the reported values of average power are overestimated.

[1]The time considered here is not the whole etching time, as for the calculations to be indicative. More information on the etching time can be found in Appendix C.

In Figure 4.3 is presented the writing scheme used to process 3 bits of the p-type Si wafer, with a grid step of 1×1 μm. The samples have been sent to the antimatter laboratory at the University of Trento to perform positron annihilation spectroscopy (PAS, see Appendix A). The samples were then etched to grow the nanochannels and PAS measurements were repeated.

Batch n°2

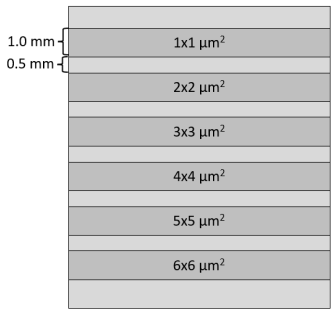

Figure 4.4: The processing scheme for the study of different grid densities is reported. [Processing performed by M. Demesh, NTNU.]

The processing of Batch n°1 was done with a grid step of 1×1 μm. As reported in section 2.3.2, a dense processing leads a pulse to influence the next in the sequence by changing the refractive index of the material after the writing. This was not known when we produced the first batch (reported in Figure 4.3). After characterization with SEM of Batch n°1 (see Section 4.2.1) new processing became necessary to study the behaviour at different densities. Different inscription densities have been explored by writing different grid patterns in a p-Si (100) 0.17-0.23 cm sample, with steps from 1 μm to 6 μm. The laser parameters have been kept constant during the writing and for the different grids in order to aim at ∼5 μm of depth. After writing, one side was lapped to expose the cross section and observe the processed depth. The 6 grid patterns have been written in a total of 3 samples (plus 3 identical copies), that have been produced with slightly different laser parameters. We call the samples S1, S2, S3, and the exact copies S1-copy, S2-copy, S3-copy respectively.

4.2.1 SEM of laser-processed samples

Batch n°1

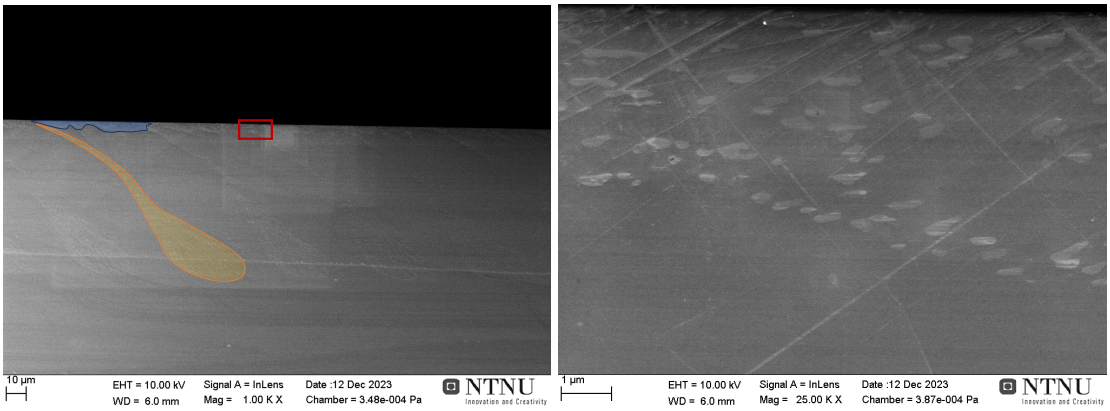

Figure 4.5: We report the two SEM images of T1. On the left: a general overview of the modified area is shown. The basic block of the repeating structure is highlighted with colors. In blue: the surface laser induced modifications. In orange: the laser induced modifications extend inside the bulk for almost 80 µm. On the right: a magnification of the red rectangle is reported. The volumes modified by the laser are clearly visible.

Sample T1 was produced with a grid pattern of 1×1 µm. Figure 4.5 reports the SEM images of the cross section of T1. The sample was produced by introducing laser pulses from the bottom (taking as a reference the orientation in Figure 4.5) and focusing them at an expected depth of 8.65 µm. The pictures clearly show that laser induced modifications in silicon are visible under SEM when a dense pattern is written (multiple pulse regime, see Section 2.3.2). A modified volume is present both near the surface (blue area) and deep in the sample (orange area). Multiple layers (up to 3) of modifications are present at different depth z but at the same (x, y) coordinates, even though we were expecting to produce a single pulse for each (x, y) coordinate. Nevertheless, a relatively high density of subsurface modifications has been produced <1 µm deep; although they do not appear to have generated a wide connected modified volume. The domain of the modified volume looks sharply defined, with a clear border that separates it from the crystalline matrix. This observation is promising for the etching selectivity of the modifications, and for a

high quality production of the nanochannels, which require a crystalline substrate to grow. Samples T1 and T2 have not been imaged with SEM yet. Even though the samples have been etched with nanochannels, an untouched area is available for future characterizations.

Batch n°2

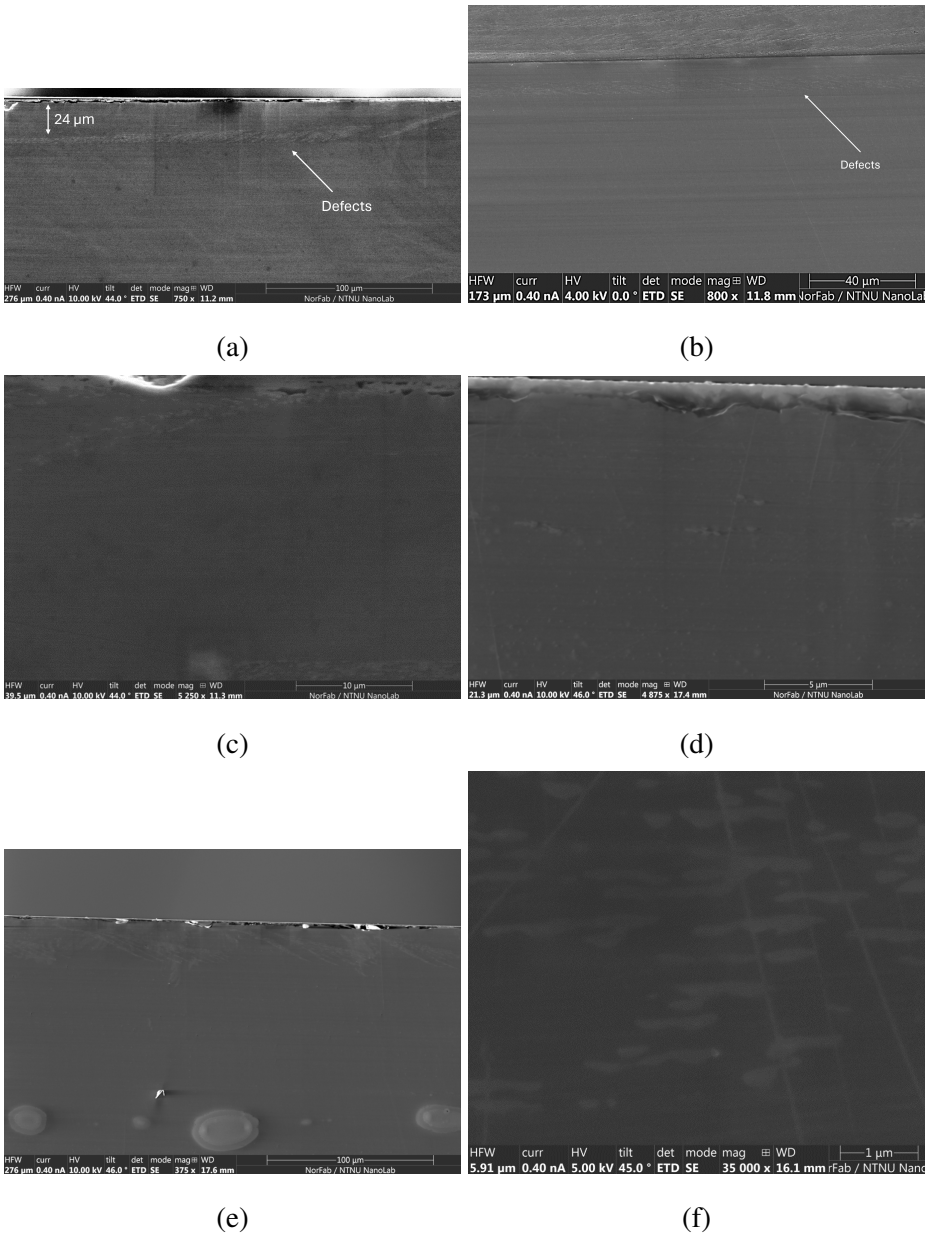

Figure 4.6: SEM images of characteristic features obtained from Batch n°2 are reported. (a) S3 grid 1×1 µm^2 presents laser modifications that stabilizes at around 24 µm of depth. (b) The copy of S3 grid 1×1 µm^2 presents the same features, showing that the samples are reproducible. (c) Same sample, at the border of the written layer the depth jumps abruptly to the surface. (d) The whole written area of S1 grid 2×2 µm^2 presents the reported feature. The modifications are not spaced 2 µm as expected, the spacing is 5 µm instead. (e) S1 grid 1×1 µm^2 presents a periodic structure. (f) We report a focus on modifications from S3 grid 1×1 µm^2.

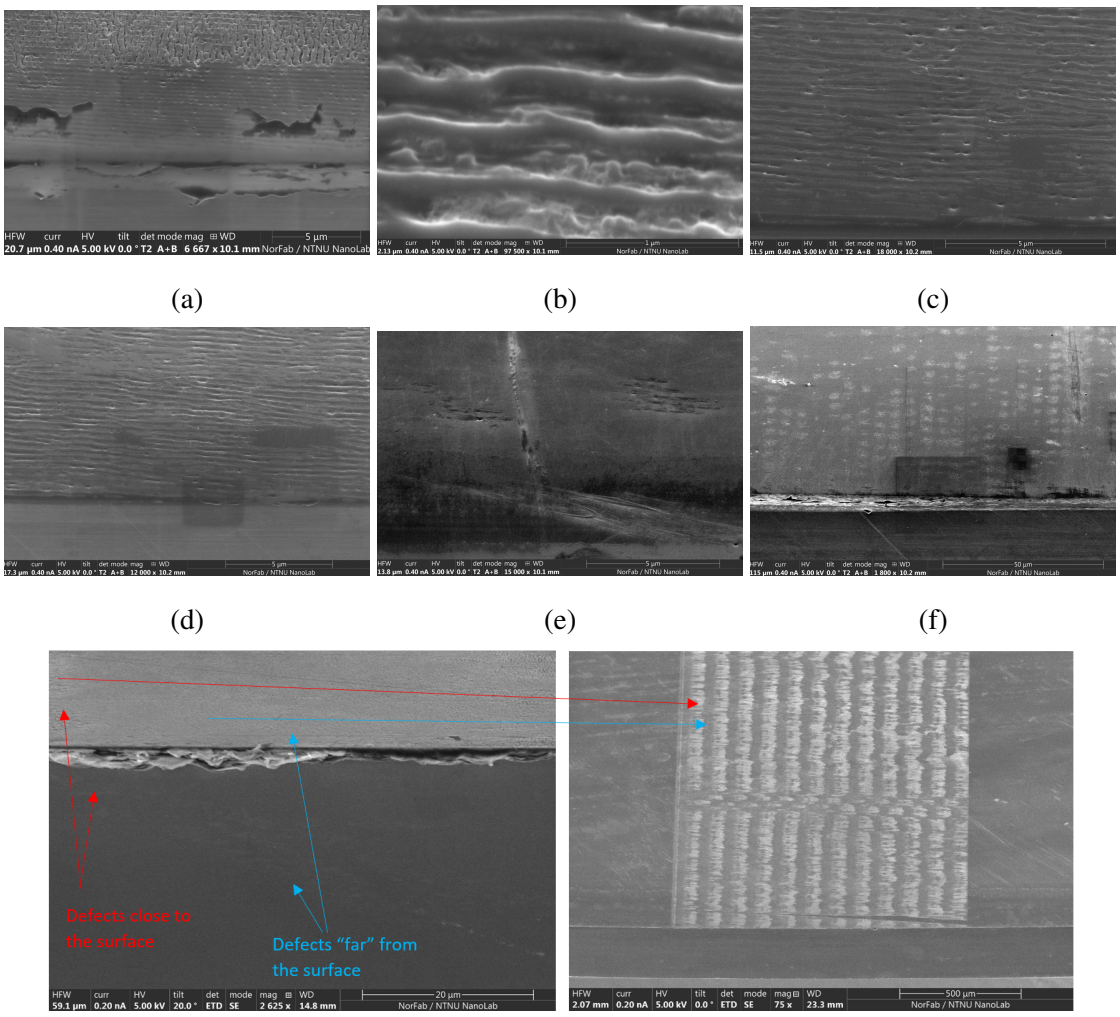

Figure 4.7: SEM images of the surfaces of sample S3 are reported. In order we can see the pattern that the different grid processing have inscribed on the surface (a) 1×1 µm^2, (b) 2×2 µm^2, (c) 3×3 µm^2, (d) 4×4 µm^2, (e) 5×5 µm^2, (f) 6×6 µm^2. (g) S1 grid 1×1 µm^2 is shown here, imaged at 45° angle. We can observe the in-bulk and the surface modifications at the same time. When the surface is damaged, the modifications are not present in the bulk, while when processing is done within the bulk, the surface is unaffected. The surface pattern can be observed repeating with regularity on the surface.

The samples from the second batch have revealed that laser written structure is distinguishable with SEM only up to 2×2 µm^2. This does not necessarily mean that in different grids we were unable to write in the bulk. As visible by comparing Figure 4.6d (a processing

with grid of 2×2 μm^2) and Figure 4.6f (a processing with grid of 1×1 μm^2) the imaging of low writing density is not easy, and a better characterization with SEM or IRM could allow us to characterize better low density written samples. What is clear, though, is that a dense grid is needed to obtain a high density of laser induced modifications, which is key for our application. However, when the density is high, it is not clear yet how to tune the laser parameters to obtain a processing uniform in depth. Figure 4.6e shows the processing of sample S1 with grid 1×1 μm^2. The written structure is dense and a repeating structure is visible, however the laser modifications are distributed in a wide interval of depths ($\sim$20 μm). Figure 4.6a reports the SEM image of sample S3 grid 1×1 μm^2, and it shows that with certain laser parameters it is possible to obtain a uniform and long ($>$150 μm) structure of laser modifications. Moreover, Figure 4.6b reports the copy made of the same sample and with the same laser parameters, showing that the produced structure is reproducible. Figure 4.6c shows that even here the written structure is not extending at the same depth for the whole processed area. In constant intervals we can observe the written structure ”jump” abruptly from deep in the bulk to the surface. A close inspection of the induced modifications show that the modified volumes are elongated in the direction perpendicular to the laser propagation (see Figure 4.6e. The surface of the samples was also inspected (see Figure 4.7. All the written grid densities present damages at the surface of the samples. ULDW produces a grating-like pattern on the surfaces with periods of some hundreds of nanometers. White light is in fact diffracted by these structures. Figure 4.7g reports a wide view of the 1×1 μm^2 grid of S1, where a periodic structure is visible. A higher magnification reveals that the brighter parts are correlated to damages at the surface while the darker areas are related to a generation of defects deep in the bulk. The observation of these samples is suggesting that if a pulse is not completely absorbed at the focal spot, the remaining energy can be deposited at other depths, be released at the surface, or be lost over the surface.

4.2.2 Positron annihilation spectroscopy of the laser-processed samples

Batch n°1

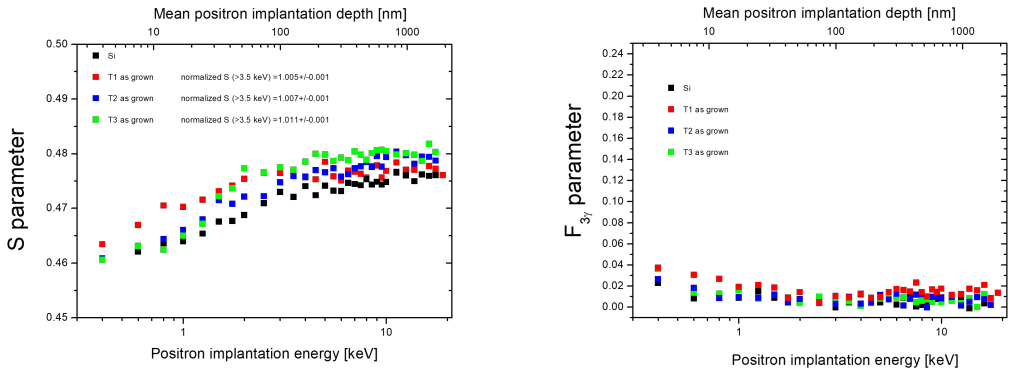

Figure 4.8: We report the results of the PAS performed on T1, T2, T3, and a reference dummy sample. (a) The S-parameters increases the nearer the aimed focus of the laser was to the surface. (b) Without nanochannels the $F_{3\gamma}$-parameter is almost zero, and no useful yield of Ps is obtained. [The measurements have been performed by Dr. S. Mariazzi, UNITN]

Before growing the nanochannels, the samples T1, T2, and T3 have been analyzed with Positron Annihilation Spectroscopy (PAS) at UNITN with the SURF apparatus, which provides a continuous slow positron beam with energies up to 20 keV. A more exhaustive explanation of PAS can be found in Appendix A. The analysis was done to study the presence of defects in the first 2 µm from the surface. The depth is limited by the maximum energy of the positron beam (20 keV). For T2 and T3 it is not possible to control the 2 mm positron beam spot to individually target the different regions within the same sample (see Figure 4.3); as a consequence, the data obtained for T2 and T3 is the result of a generally targeted area in the sample. While, for T1 the signal is most surely given by the modified region given the wider area that could be targeted. The measurements are reported in Figure 4.8.

As anticipated, we expected the modifications to be at lower depths for the different targets, with deeper processing for T1, and most superficial for T3. However, the SEM

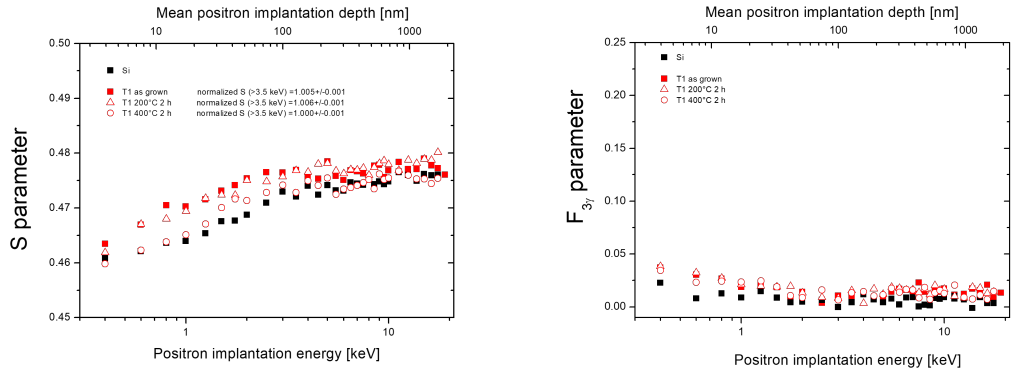

Figure 4.9: Here are presented the results of PAS performed on T1 after each of the thermal cycles. (a) The defects present at the surface slowly disappear the higher the temperature of the thermal anneal. [The measurements have been performed by Dr. S. Mariazzi, UNITN]

images taken of T1 (see Figure 4.5) and images taken of both T1 and T2 after the electrochemical etching step (see Figure 4.12 and Figure 4.13), show that laser modifications are always present near the surface. Hence, we are sure that the modified volumes have been probed by PAS. The measurements indicate an increasing trend in the S-parameter as the laser processing became more superficial. We recall that a high S value is related to a high concentration of lattice defects (see Appendix A). The observed values of S are compatible with monovacancies or small vacancy clusters [32]. A possible explanation is that the laser-induced modifications are, as expected, introducing defects in the from of mono or multiple vacancies, or nanovoids. Note that a highly crystalline surface layer is fundamental to grow nanochannels of the desired diameter; however, the laser processing affects the samples up until the surface. In fact, compared to an unprocessed silicon sample taken as a reference from the same wafer, all the processed samples present a higher value of S in the first 100 nm. We wanted to explore the possibility of obtaining clusters of defects by heating the processed samples to high temperatures. Hence, sample T1 went through some cycles of thermal annealing at 200 °C and 400 °C in a vacuum oven for 2 h. After each cycle new measurements with PAS were performed to follow any change. A summary is reported in the Figure4.9. A visible trend in the S-parameter suggests that the thermal treatments anneal the defects without a complete reabsorption

of the modified area. After the thermal treatment, the first 100 nm assume comparable S-values with the unprocessed silicon, almost cleaning this area from any induced defect in the lattice. Laser-written structures are reported to be erasable following exposure to high temperatures (1100 °C) in an oven for 2 h [4]. Hence, the thermal cycles on T1 may have allowed the stress surrounding the laser modifications to be relaxed, without erasing the laser modifications themselves.

4.3 Inductively Coupled Plasma-Reactive Ion Etching

The target requires the cavities to be embedded in the sample at a depth $<$500 µm. However, we are not able to produce laser modifications at that small depth with good uniformity and without damaging the surface. Thus, the best approach is to produce the laser-induced modifications far from the surface and use an etching technique to remove the excess material. To achieve a high precision, we used a technique called Inductively Coupled Plasma-Reactive Ion Etching, that makes use of a chemically reactive plasma to remove material. We have tested two different recipes:

1. SF6/O2:95/100: sccm 17 mTorr, ICP power 575 W, RF power 25 W, Etch Rate 2000 nm/min. Non-isotropic.

2. CHF3/SF6:50/15: sscm 15 mTorr, ICP power 1200 W, RF power 30 W, Etch rate 1600 nm/min. Isotropic.

4.3.1 SEM of ICP-RIE processed sample

Batch n°2

Sample S3 has been used to test the efficacy of ICP-RIE on our substrate. S3 has been chosen because of the well defined layer of defects in the 1×1 µm^2 grid. The originally processed depth was 24 µm as visible in Figure 4.6a. The sample was exposed to a first ICP-RIE step using the 1^{st} recipe for 60 s. With an etching rate of 2000 nm/s we have indeed removed 2 µm from the surface (see Figure 4.10a). The etching step has enhanced the presence of the laser modifications that appear clearer under SEM, probably because

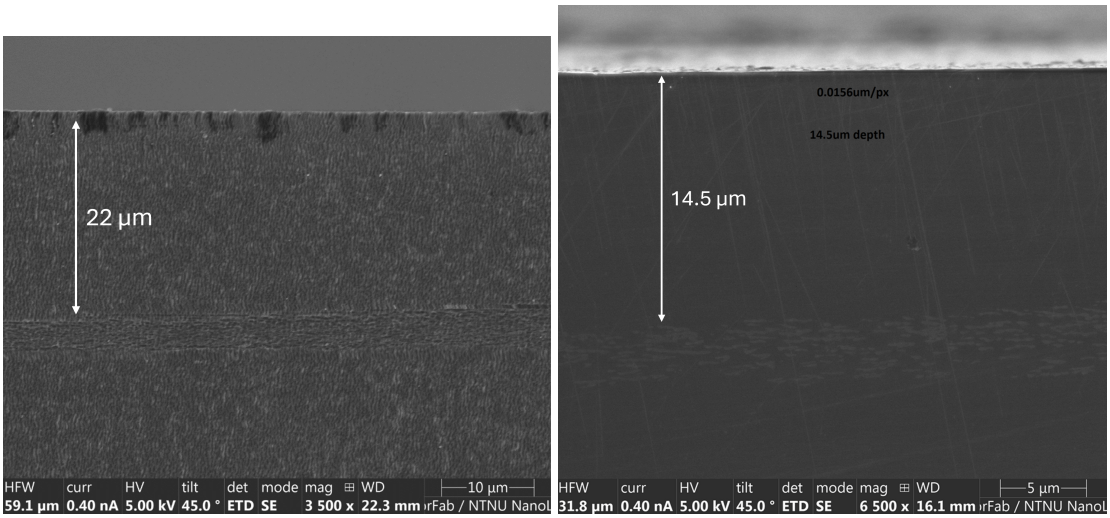

(a) (b)

Figure 4.10: Sample S3 was exposed to two ICP-RIE steps, the first reported in (a), and the second reported in (b).

of the nonisotropicity of the recipe used. A second step of ICP-RIE have been run with the 2^{nd} recipe, which is instead isotropic, for a duration of around 270s (time not sharply known because of malfunctioning of the instrument) reaching a final depth of the laser modifications of 14.5 µm. In Figure 4.10b the lapped cross section after the second ICP-RIE step is reported. Although both recipes are effective in removing excess material, the isotropic recipe is also effective in removing the surface imperfections. Moreover, the etching rate of the isotropic recipe is also slower, thus giving a higher resolution in controlling the amount of removed material. The precision of the technique allows for the removal to be controlled by tens of nanometres, enough for our application.

4.4 Electrochemical etching

Most of the processed samples have been electrochemically etched to produce nanochannels that go from the surface to the laser-modified region and over. The etching has been performed also on an additional dummy silicon sample taken from the same wafer to serve as a reference. Referring to previous experience in growing nanochannels on a similar substrate[15], to obtain nanochannels with a diameter of around 8 nm and a length of $\sim 2\,\mu m$

the following parameters have been set: commercial aqueous solution at 48% of HF with volume ratio 1:3=HF:ethanol, 10 mA/c^2m etching current, and 15 min etching time, followed by at least 2 h oxidation time. The oxidation time is fundamental to grow a film of few nanometres of SiO_2 over the whole surface exposed to air, which plays a key role in the e^+-Ps conversion [13].

In order to assess whether the nanochannels can still grow in the presence of laser-induced stress, and if there are any signs of open cavities, we proceed to image with SEM the targets' cross section. We have noticed that the structures are strong enough to cut the sampled with a diamond tip. Subsequently, consecutive lapping steps were applied with progressively smaller diamond-particle decorated films (with sizes of 30 µm, 9 µm, 3 µm and 1 µm).

4.4.1 SEM of the etched targets

Batch n°1

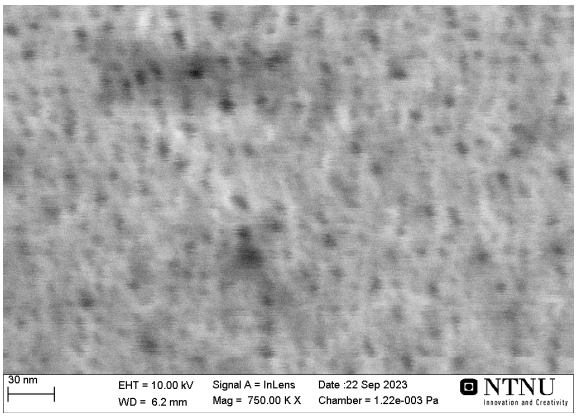

Figure 4.11: We report the top view of the electrochemically etched surface of the dummy sample of silicon. The nanochannel's diameter is $\sim$ 10 nm proving that the used substrate is suitable for producing nanochannels of the required size. [Figure from private communication with E. Einmo, NTNU]

In Figure 4.11 we report the top view of a dummy sample taken from the same wafer of the other samples after ECE. Holes of $\sim$10 nm of diameter confirms that the substrate is suitable for producing nanochannels of the required size for our application. In Figure

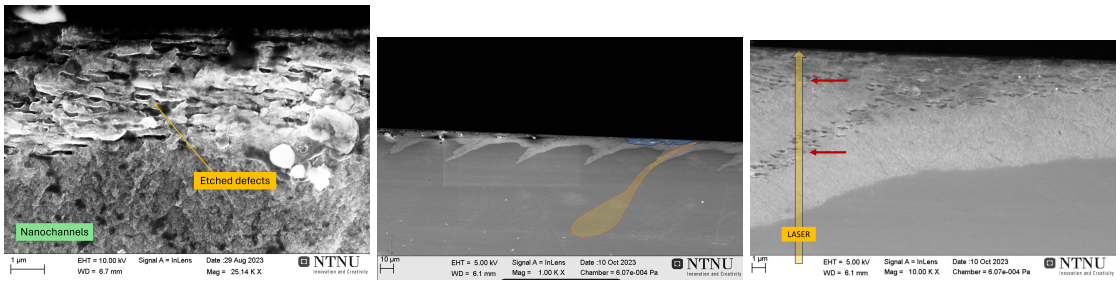

(a) (b) (c)

Figure 4.12: SEM images of T1 after electrochemical etching (ECE) are reported. (a) Without lapping, embedded cavities are present and seem open and hollow. Maybe even connected among them. Their shape resembles the shape of the laser modifications observed before the ECE. (b) The general structure observed before ECE (Figure 4.5) is partially highlighted by ECE as the nanochanneled area appears brighter. The etching happens at triple the rate in the modified volume, compared to the crystalline matrix. (c) A closer look to the etched modifications confirms the presence of many layers of laser modifications, pointed with red arrows. [Figures from private communication with E. Einmo, NTNU]

4.12 and Figure 4.13 SEM pictures of the electrochemically etched T1 and T2 respectively are reported. It is possible to distinguish the volume where the nanochannels grew on the crystalline substrate as the color appears brighter. The volumes modified by the laser-induced modifications present cavities embedded in the sample, which appear hollow. They appear hundreds of nanometers tall and few micrometers wide. The shape of the cavities is the same as the shape of the laser modified volumes before the electrochemical etching 4.5 suggesting that the etching selectivity of silicon processed with ULDW is high. In the dummy, the cross section of the nanochannels is visibly starting from the surface and reaching a depth of more than 6 µm, while in the processed samples ECE etches until $>$15 µm. Thus, the etching rate of the processed area is 3 times faster than the processing of the untouched part of the sample. Moreover, if we consider that a considerable part of the ULDW processed volume still looks crystalline, we can state that the etching rate of the ”bubbles” of laser modified volume is at least around one order of magnitude higher than bulk crystalline silicon. The etched volume follows the written structure of

the laser modifications due to the difference in etching selectivity. At the bottom of the etched layer, the laser modifications are still visible. In Figure 4.12c the different layers of writing appear even clearer after ECE , and we can see that the cavities are connected by nanochannels grown in between.

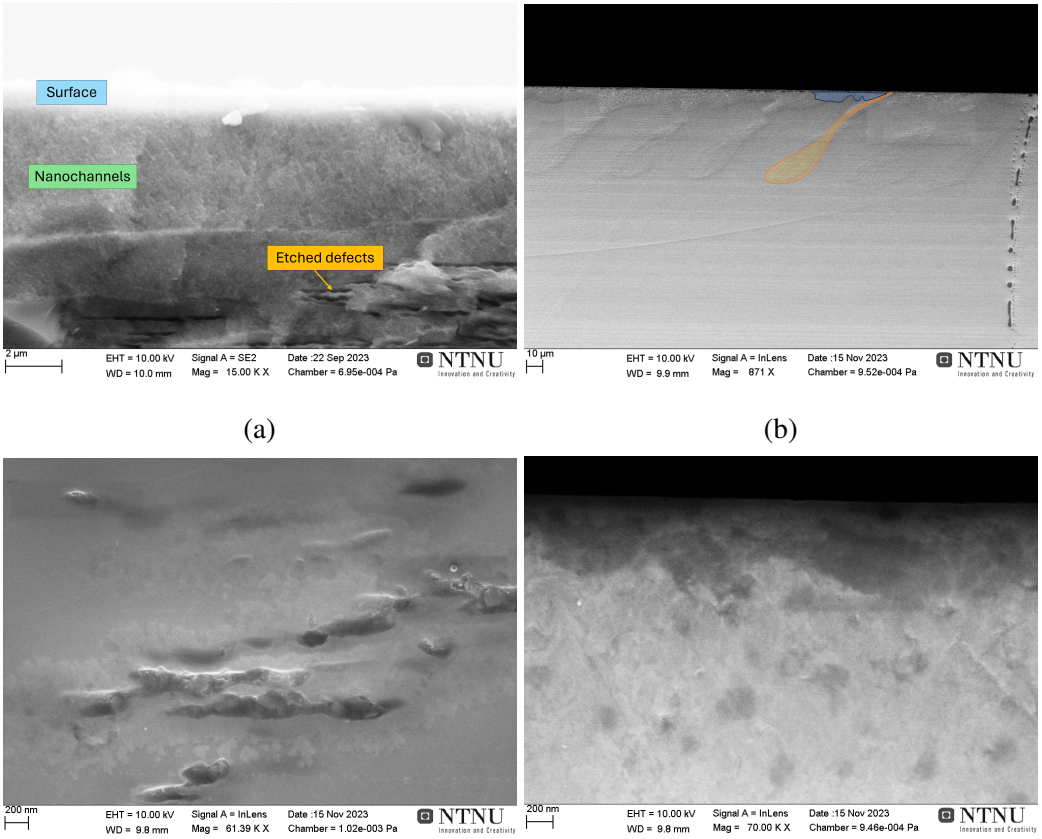

(a) (b)

(c) (d)

Figure 4.13: SEM images of T2 after electrochemical etching (ECE) are reported. (a) Without lapping, embedded cavities are present and seem open and hollow. Many cavities are also connected. Their shape resembles the shape of the laser modifications observed before the ECE. (b) The general structure observed before ECE (Figure 4.5) in sample T1 is found also in sample T2 (c) A close look to some etched cavities. They are $\sim$200 nm tall and $\sim$1 µm wide. (d) The subsurface cavities are observed with higher magnification. [Figures from private communication with E. Einmo, NTNU]

Batch n°2

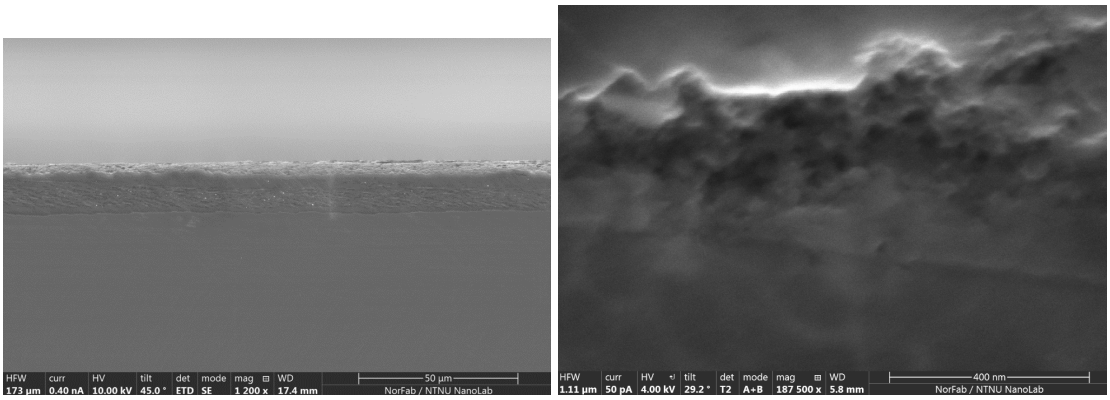

Figure 4.14: ECE of sample S3. (a) The general view of the etched sample is reported. (b) A magnification on an isolated etched modification is shown.

After the ICP-RIE etching step on S3, the depth of the laser modification in the 1×1 µm^2 grid was reduced to 14.5 µm (see Figure 4.10b). The electrochemical etching step was performed on S3 as visible in Figure 4.14. The uniformity of the written structure has been maintained even after ECE. A focus on an isolated modification shows a cavity like structure.

4.4.2 Positron annihilation spectroscopy of the electrochemically etched samples

Batch n°1

PAS of the samples T1, T2, and T3 was performed to explore the Ps yield [2]. The results are reported in Figure 4.15 alongside the measurements performed on a dummy sample taken from the same wafer as a reference. This time the S-parameter results abundantly higher than bare silicon, suggesting the presence of structures with wider open volumes. This is

[2]The measurements were done prior to SEM characterization of the samples, and the conclusions drawn with blind knowledge of the laser processing appearance.

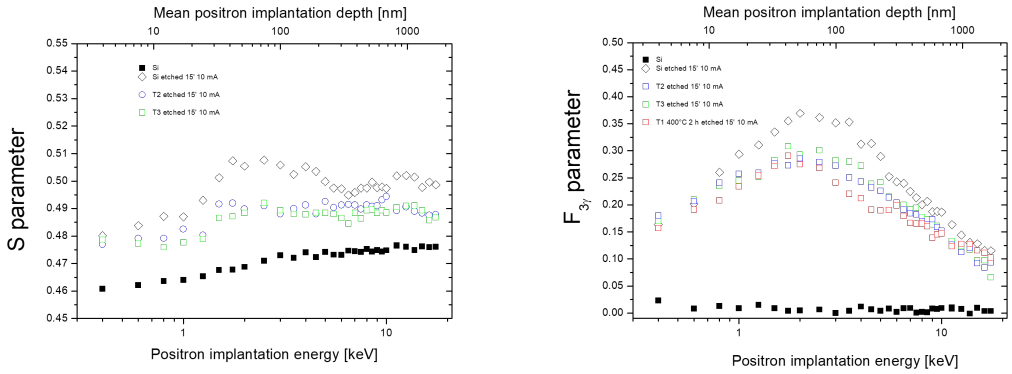

Figure 4.15: Positron spectroscopy of electrochemically etched T1, T2, T3, and dummy. Non-etched dummy as a reference in black. (a) The S-parameter increased compared to non-etched dummy. (b) The $F_3\gamma$-parameter shows the presence of a high yield of positronium, with a visibly lower yield for the laser-processed samples. [The measurements have been performed by Dr. S. Mariazzi, UNITN]

confirmed by the high yield of Ps. In fact, the $F_{3\gamma}$-parameter, that is related to the production of positronium, shows that the produced targets are able to convert the positrons in positronium. The etched dummy shows the characteristic $F_{3\gamma}$ profile of a converter with nanochannels connected to the surface with a depth of around 1 µm. The maximum fraction of emitted Ps is linked to an implantation energy of 1-2 keV. At high energy, $F_{3\gamma}$ decreases because fewer Ps particles manage to reach the surface and undergo pick-off annihilation. The decrease in the $F_{3\gamma}$ at low energy is due to the lower Ps formation close to the surface and the high emission velocity of the formed Ps [33]. This allows a significant portion of Ps to escape far from the detector, resulting in lower detection efficiency. The decrease in Ps in the samples previously treated with the laser (T1, T2, T3) could be attributed to either:

- The irregular growth of the nanochannels caused by the presence of stress and changes in resistivity induced by the laser;
- The existence of buried volumes where the Ps gets trapped and, unable to reach the vacuum, undergoes pick-off annihilation, not contributing to the $F_{3\gamma}$-parameter.

A closer look at the sub-surface cavities reported in Figure 4.13d gives credit to the

presence of buried volumes few hundreds of nanometres from the surface.

4.5 Conclusions

To sum up, we have studied subsurface micron-sized laser modifications in silicon for such important future application as positronium BEC formation in a hollow silicon cavity. For the first time, we could create a hollow volume inside silicon that is connected to the surface by a comb of nanochannels. A good production of positronium has been achieved, which holds promise for the usability of the new hollow cavity in future positronium BEC creation. More specifically:

- ULDW can be used to inscribe regions of modified volumes in the bulk of crystalline silicon at a defined and constant depth, with an extension $>$250 µm. The processing is reliable and replicable, and produces a high density of laser induced modification. The laser induced modifications appear dense in lattice defects, mono and multi vacancies.

- Thermal annealing can be used to partially remove defects within the lattice without removing the laser induced modifications. The thermal treatment (up to 400°C) does not remove the laser induced modifications and it does not alter the etching selectivity of the modified volumes.

- ULDW alters the silicon lattice forming volumes with high etching selectivity compared to the lattice matrix. After elecrochemical etching, the laser induced modifications appear excavated and hollow, keeping the shape they had prior to the etching. The hollow volumes are $\sim$200 nm tall and some µm wide, and are connected by nanochannels. The nanochannels appear to have formed correctly in the ECE processed samples, and a good production of positronium have been achieved.

- The produced targets are capable of high e^+-Ps conversion, but the lower yield compared to pure nanochannels need further investigations. The employment of different etchants and hybrid techniques that use varying currents during the electrochem-

ical etching of the samples may be explored in the future to assess the possibility to generate micrometre-sized hollow structures.

5. MALTA2: Introduction and Motivation

5.1 The MALTA2 chip

5.1.1 Design

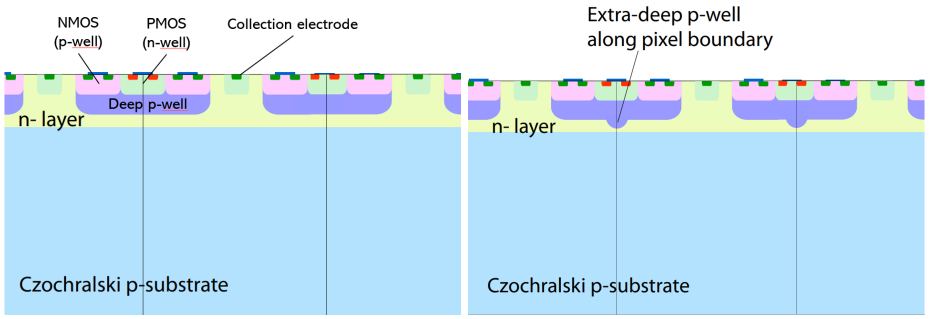

(a) (b)

Figure 5.1: (a) Cross section of the MALTA2 pixel sensor. It presents a continuous low dose n-layer on Czochralski p-substrate. The black vertical lines indicate adjacent pixels.(b) An additional deep p-well is present to increase the lateral gradient of the field[34].

The MALTA2 chip is a Depleted Monolithic Active Pixel Sensor (DMAPS) developed in the Tower Semiconductor 180 nm CMOS imaging process, and it has been designed as a candidate for the ATLAS Inner Tracking upgrade Phase-II at the HL-LHC and for future collider experiments[1]. The chip has a monolithic architecture that combines the pixel sensor and front-end in a single piece of silicon which reduces its material budget and improves tracking performance. Figure 5.1 shows the cross section of the implant design of MALTA2. On top of the implant, a metal circuitry connects the transistors and completes the CMOS architecture. The implant develops in silicon in the first micrometers from the surface, and is encapsulated in a highly doped deep p-well. The ionisation signal is collected on the small n-well collection electrode in the pixel center (3.5 µm diameter).

[1] All the information regarding the MALTA2 tracking sensor have reference in [34] if not stated otherwise.

The electrode is connected to the analog front end, located together with the digital in-pixel circuitry in the surrounding deep p-well. The deep p-well is embedded in a low-dose n-type layer across the full pixel matrix; while under it, a Czochralski p-substrate is found until the back side. The n-layer generates the depletion of the silicon sensor, and separates the deep p-well of the pixel circuit from the p-substrate. The n-type implant improves the depletion of the sensor volume. In its absence, the depleted volume would form around the collection diode like a bubble, and the edges of the pixel would be very hard to deplete. The n-layer allows the depletion layer to expand from the interface between the n-layer and the p-substrate in a uniform way across the whole pixel. The p-substrate is reverse biased between $-6\,\mathrm{V}$ and $-50\,\mathrm{V}$ depending on the radiation dose it received, the higher the dose, the lower the voltage; this causes the depletion of the high-resistivity ($3\,\mathrm{k\Omega cm}$) Czochralski substrate bulk. The p-well is biased at $-6\,\mathrm{V}$. The n-layer is depleted from its junctions to the deep-p-well on one side and p-substrate on the other side. The depletion width is estimated to be $>50\,\mu\mathrm{m}$,even though it can vary depending on the applied bias voltage and the irradiation damage of the silicon bulk. . As for last, 1 V voltage is applied to the collection electrode.

5.1.2 Operation

When an ionizing particle passes through the chip, it deposits energy following the Landau distribution (as a correction to the Bethe-Bloch distribution for very thin materials), that shows the amount of energy deposited per length crossed, but given the thickness of $100\,\mu\mathrm{m}$ of MALTA2, the energy deposition can be considered linear. The energy deposited translates into ionization of the atoms of the silicon lattice, i.e. free charge carriers generation. To calculate the expected ionisation charge for thin sensors, we can assume an ionisation charge of 63 electron-hole pairs per $1\,\mu\mathrm{m}$ path length[35]. In the case of a MALTA2 with Cz-substrate the thickness of the depletion layer is estimated to expand over $50\,\mu\mathrm{m}$, and a most probable ionization charge of $3150\mathrm{e}^-$ is expected, well above the $200\mathrm{e}^-$ threshold detectable charge of the front-end circuit. The produced charge is the signal to be detected, so the charge collection and processing of the readout needs to be faster than the collision rate of LHC of 40 MHz.

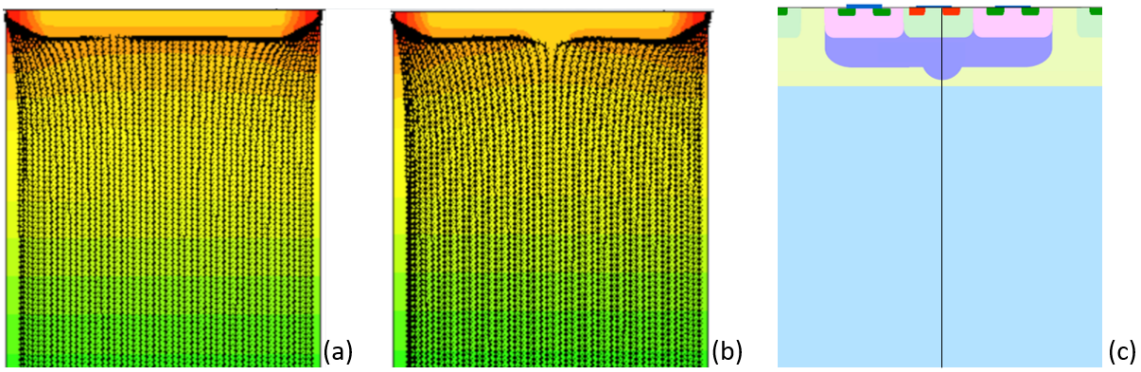

Figure 5.2: Electrostatic potential and electric field lines obtained from TCAD simulations of the 150 µm thick Cz-sensor with continuous n-layer (a) and of the Cz-sensor with extra deep p-well (b). Working voltages of 0.8 V on the collection electrode and −6 V bias on the p-well. The represented cross section is centered at the pixel edge, with the collection electrodes at the sides (c). [34]

Only the electrons generated within the depletion layer are collected through drift (as opposed to diffusion) and contribute to the signal. This is because they are surrounded by the electric field created by the reverse bias applied to the p-substrate. However, it is evident from TCAD simulations (Figure 5.2) that the electric field has a weak lateral component. Due to the small collection electrode (3.5 µm of diameter), the field configuration and charge collection under the deep p-well is critical. Compared to the 36.4 µm width of the pixel, the electrode is relatively small and electrons ionized at the pixel edges, where the horizontal field gradient is minimal, will spend a long time drifting before eventually a fraction of the generated electrons reaches the funnel like field profile of the collection electrode, thus being detected. Simulations with an additional extra-deep p-well (Figure 5.1) show the presence of a stronger lateral component of the field rising from the depletion of the p-well and n-layer interface, that allows for a lateral pull of the electrons towards the collection electrode. It is here that the ULDW comes into play. The laser-induced modifications change the lattice structure of the material, and can modify its electrical properties. Depending on the nature of the modification it may be possible to achieve a field profile equivalent to an extra deep p-well equipped MALTA2.

5.1.3 Data acquisition of MALTA2

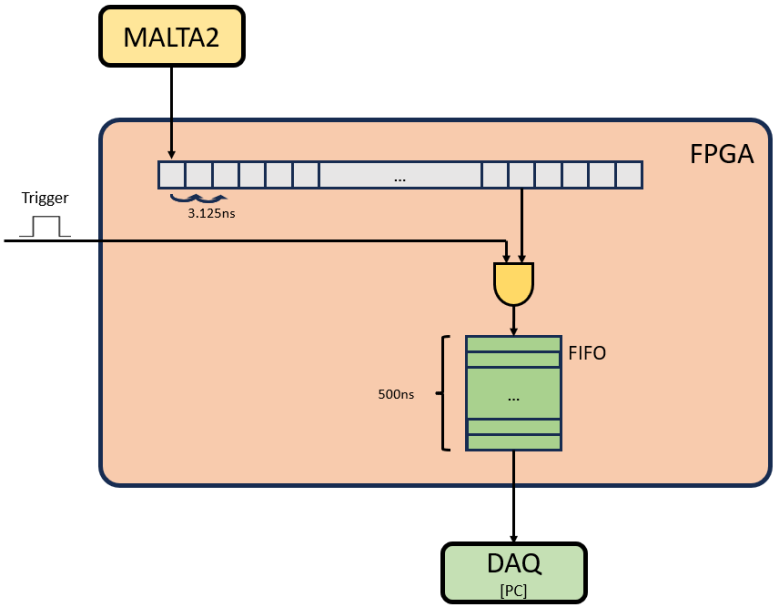

Figure 5.3: Schematics of the data acquisition from MALTA2.

For the operation and communication with MALTA2 it is required to implement the following instrumentation:

1. One MALTA2 chip mounted on a PCB
2. One Kintex-5 FPGA to manage the data acquisition from the chip
3. The voltage supply for both MALTA2 and the FPGA
4. A PC to control the boards
5. An instrument to produce the triggering signal for the FPGA. For our purpose: an oscilloscope (LeCroy Waverunner 8104).

In order to understand the requirements of the setup, it is important to clarify some of the working mechanism of the data acquisition of MALTA2. When a signal is detected at the collection diode of a pixel the readout data is transmitted to a shift register on the FPGA that can buffer data for up to 300 ns. Data is moved through the shift register at

a rate of 320 MHz which equates to timing bins of 3.125 ns. The signal from MALTA2 requires a finite time to propagate in the experimental setup. Therefore, a trigger delay can be configured by reading out from a specific position along the shift register. Once a readout trigger reaches the FPGA, a 500 n sec data frame is read out from the shift register into a FIFO. Note that for laser pulse rates larger than 2 MHz the time interval between pulses is less than 500 n sec and multiple signals may be recorded within a single readout frame. This implies that if there are two subsequent signals that are distanced by less then Δt_{FIFO} they will be considered part of the same event. This corresponds to a limit for the frequency acquisition of $f_{ACQ} = 1/\Delta t_{FIFO}$ =2 MHz. As an example, if a high repetition rate is chosen, say 8 MHz a pulse every 125ns is observed; thus, up to 5 pulses can fit in the Δt_{FIFO} =500 ns. The time stamps attached to MALTA2 data by the FPGA can only cover time intervals of a few milliseconds and are expected to overflow multiple times before the data is read out to the PC. Thus, a global time stamp for MALTA2 data cannot be reconstructed. To reconstruct the timestamp we employ the trigger ID (the unique identifier of a trigger event) as a timer. While this approach should work even at several kHz, the oscilloscope cannot handle this trigger rate, and it's likely that we are restricted to around 200 Hz or a similar rate. Hence, the oscilloscope is the constraining factor for achieving a higher pulse rate.

5.1.4 Time walk

We already discussed the mechanism of detection of a cloud of free carriers. What is important to point out now is that the pixel matrix of MALTA2 is composed of digital and analogue pixels, but the design of the PCB used in this experiment covers the analogue pixels; thus, only the digital pixels are accessible to the laser pulses. For these pixels, the output is binary, yielding either a 0 (no hit) or a 1 (hit). This outcome results from processing the analog waveform from the affected pixels through a discriminator ("detection threshold" in Figure 5.4), converting it into a standardized rectangular pulse. Consequently, all the information contained in the original analog waveform is lost at this stage. The information we are left with is the timestamp at which the binary signal was recorded, with precision of 0.39 n sec. It's crucial to note that this timestamp includes the

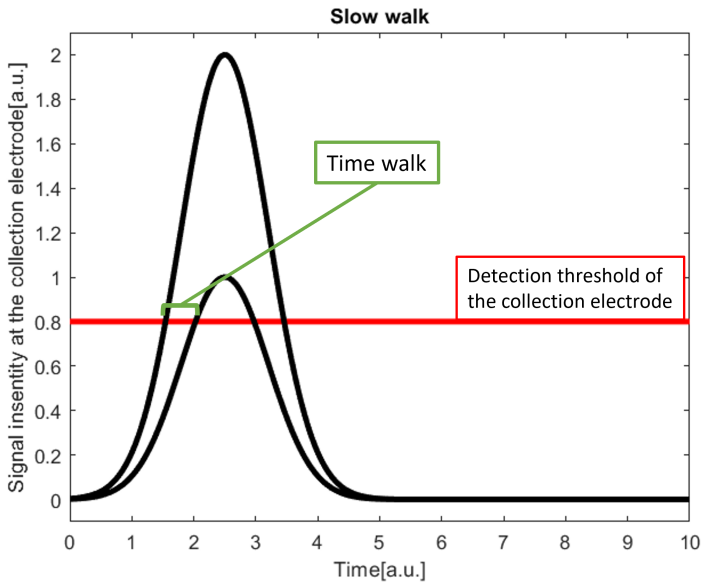

Figure 5.4: If a free carrier cloud produced by an ionizing particle is very small, but still detectable by the collection diode, it will present a delay in its detection. The signal at the collection diode can be read only if its intensity is over a given threshold, hence the rising slope of the signal plays key a role in the detection time.

time walk of the signal, and this time walk is linked to the signal's amplitude. Specifically, larger amplitude signals are recorded faster in our system. In fact, a large collected charge reaches the detection threshold earlier and is thus also recorded earlier than a small signal. This effect is called "time walk" (see Figure 5.4).

The ionization profile of the laser has a diameter of 2 µm, which means that the finite size of the laser's ionization volume can cause charge sharing between adjacent pixels. Additionally, in the z-direction, it extends over a width of ∼20 µm. If the chip is not perfectly aligned with the laser's path, the pulse may be injected at a slight angle. This can result in the charge being distributed over a broader area and potentially causing it to be divided among pixels. As a consequence, the cloud is split in two fractions, whose proportion is related to the position of the center of mass of the cloud.

The two fractions are detected separately by different pixels and the time walk of the two generated signals (see section 5.1.4) will depend on the size of the fractions. Therefore, when reconstructing the filling the pulse timing histogram (Figure 5.11) two peaks

are expected to appear separated by a time delay corresponding to the difference between the time walk of the two fractions of free carriers. However, the readout mechanics of MALTA2 may introduce an additional delay if the two triggered pixels are in the same group. In fact, the pixel matrix of MALTA2 is divided in groups of 2x8 pixels. When a pixel is triggered, the whole group is read out and the dead time of a second readout is 5 ns. Hence, if the detection of the smallest fraction of free carrier is not synchronous with the biggest fraction, the time stamp assigned to the small fraction will possess an additional 5 nsdelay.

5.2 Ultrafast Laser Direct Writing on MALTA2

Ultrafast Laser direct writing could be used to effect modifications to the electric field in the MALTA2 sensor in a way that improves charge collection and thus detection efficiency. However, several considerations must be made. From preliminary analysis the laser-induced modifications in the crystal do not get amorphized, but present lattice defects (see chapter 4.2.2). The size of the defects is still unknown, and can range from a single atom vacancy, to a cluster of defects a so called nano void. If this description is correct, the laser modifications do change the local electric properties, but might affect negatively the charge mobility.

It is known [36] that the presence of lattice defects changes the effective doping concentration N_{eff} through the creation of deep level acceptors and donor traps. It happens for highly irradiated MALTA2 chip[37], that the non-ionising energy loss from hadron irradiation generates lattice defects causing the effective p-type doping of the high-resistivity bulk to increase, and it also reduces the effective doping of the n-layer. The change in the N_{eff} requires a high reverse bias to be applied on the p-substrate to cope with the loss of trapped electrons that make up the signal. From an example calculation on sensors of the same family of MALTA2, while for an unirradiated chip with resistivity 3 kΩcm the application of a reverse bias of -50 V leads a calculated depletion thickness of 110 µm, for a sensor irradiated with $2 \times 10^{15} n_{eq}/cm^2$ and resistivity 150 Ωcm the depletion thickness is instead 25 µm[34].

Consequently, the inscription of laser-induced defects might shape the electric field gradient on the pixel edges to increase the efficiency in the charge collection, but with the side effect of generating losses due to electron traps in the defected volume. In the case of MALTA2 the modified volume placement was envisioned in two flavours(Figure 5.5), with modifications right under the collection electrode or at the pixel edges. Defects under the collection electrode would need to give a similar effect to n-doping , thus modifying the depletion layer to enhance the lateral attraction towards the center of the pixel. While, for the modifications at the pixel edges to work, they should generate a p-doped volume (as suggested by the radiation damaged chip) to push the electrons towards the central part of the pixel, where the collection electrode is situated.

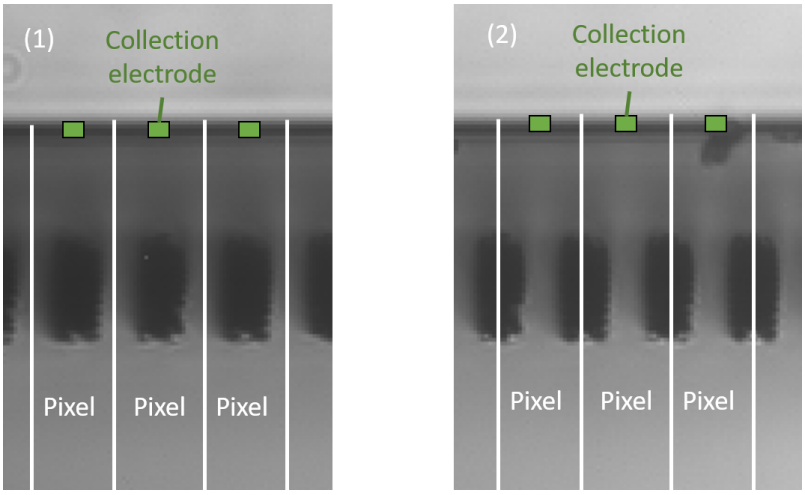

Figure 5.5: The two flavours of laser processing are presented on an IR image of an attempt in MALTA2. The first presents the modifications right under the collection electrode, while the second have the modifications at the pixel edges. [Processing and images provided by M. Demesh, NTNU.]

Processing attempts

Dummy samples (see Figure 5.6a) were used to make modifications of the Cz p-substrate of MALTA2 at different depths (see ch.2.2) in order to find the best working optical parameters. A first attempt was performed on a working chip (the chip was proven to be working before it was sent to NTNU) processing the volume at the pixel edges (see Figure

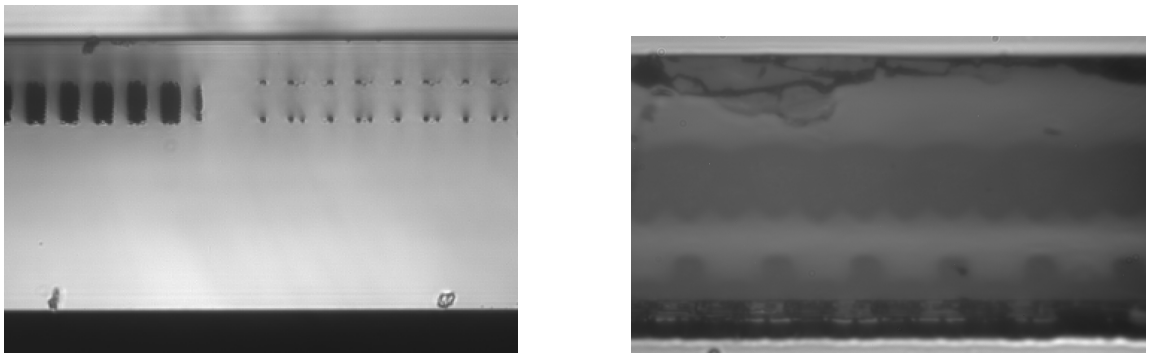

(a) (b)

Figure 5.6: (a) Shown is the cross section of an processed dummy MALTA2. At the right are made clear the edges between which the volume have been modified, with maximum depth of ∼80 µm from the bottom. At the left, the full volume is modified. The bottom surface does not present the metallic circuitry of MALTA2 since it is a dummy, and no signs of back reflection are visible. (b) Shown is the cross section of an processed MALTA2 chip. The metallic layers of the circuitry are at the bottom. The same chip was imaged with optical microscopy and reported in Figure 2.7b. Albeit the writing at mid-depth was successful, at the bottom the signs of back reflection that have damaged the CMOS are evident. [Processing and images provided by M. Demesh, NTNU.]

5.5, and Figure 5.6b). The inscription was successful, but when tested again, the chip was not operational. An inspection with IR microscopy has shown signs of back reflection (see Figure2.7b). Likely the back-reflections on the CMOS metals caused defects in the CMOS implants and broke the chip. Of course, any other reasons for a broken chip cannot be excluded, like physical damage from handling, electric discharge, etc. To assess the reasons behind the broken chip, the silicon surface of the chip was mapped with optical microscopy. The images have shown that the processing that should have been done at a depth of 80 µm where present at the back surface suggesting that the written depth was not constant across the chip. On a chip thickness of 100 µm we expect fluctuations in the written depth of 10 to 20 micrometres. The much larger observed change in written depth could be due to:

1. the chip is bent from the beginning, before processing

2. the chip is bent while writing due to stresses caused by the written modifications

3. the chip is not bent, but the laser processing is not uniform (maybe due to laser losing power in time or the changes in the focal depth)

4. during the writing process, the chip is tilted by a piece of dust and is not perfectly orthogonal to the laser

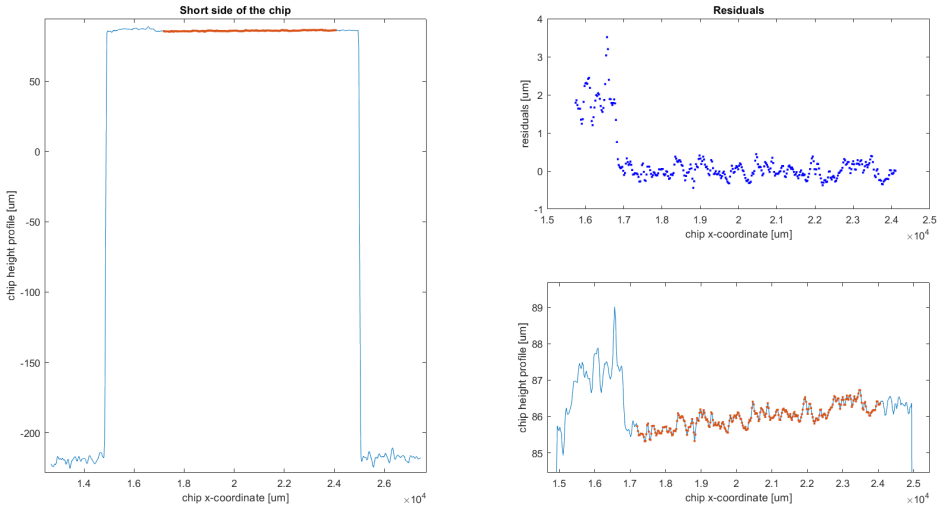

Figure 5.7: The height profile of the short edge of chip W8R22 is presented here. The orange points have been used to remove the background inclination and visualize the fluctuations in height.

(1) Regarding the first point we now know that most probably the chips are straight. The short and long side of two MALTA2 chips (W8R21, and W8R22) have been scanned with an optical scanner that returns the value of the height profile (Figure5.7). To check the straightness of the height profile, it is sufficient to select the most linear part of the profile (orange in the figure), and use it as a reference to eliminate the background inclination of the chip that can be given for example by a piece of dust on one side of the chip. Eliminating the contribution of the background tilting, it is possible to visualize the fluctuations on the overall thickness. In Figure5.7 it is reported the scanned profile of the short side of MALTA2 W8R22, which has the biggest fluctuations measured of less then 4 µm. To conclude, we were looking for bending in the order of 10-20um to assign the

observations to a bent chip. (2) Unfortunately, no data is available for a processed chip. (3) The laser was noticed to lose power in time, most probably attributable to thermal heating of the optical components. Since the first chip was processed on the whole pixel matrix, the effects of the laser losing power might indeed explain the observed change in focal depth. To be mentioned here is that the laser was further stabilized for the new processing. 4) From the height profile it is visible how the chip, even if it seems straight, was evidently bent by a piece of dust even in a clean room ISO 5, where the height profile was taken. The laser processing is done in an open laboratory and dust might cause the tilting. From the height profile measurements we can conclude that even in a ISO5 clean room, the maximum height different due to inclination of the long side of MALTA2 was measured to be around 5 µm. In an open laboratory this might be one of the reasons for the nonuniform processing. However, a tilted DUT is not fundamentally a problem since it is the DUT that is aligned with the laser, not the stage on which it sits.

Further attempts have seen the processing of smaller areas to avoid overall changes in the written depth. Unfortunately, they always turned out to be broken, and imaging still have to be performed to assess the cause.

5.2.1 Suggested improvements to the setup and sample processing

Given that this was a proof of concept, more than a final processing itself, we can distillate some positive feedback from the attempts performed so far. It seems necessary to improve the setup to accommodate the required precision in terms of alignment of the laser to the sample on the x-y position. For example in this application it is fundamental to be sure that the modifications are done at the desired position in the sensor volume with sufficient precision. As it will be evident later on (see chapter 5.3) the implementation of an infrared camera within the setup to have a real time control on the aiming position of the laser could unlock higher precision in the processing. The cleanliness of the lab to perform these type of measurements may be fundamental to avoid bending of very thin samples that might not result perfectly flat if one edge is lifted by a grain of dust.

In conclusion, we do not have any promising result regarding a direct modification of

MALTA2 to shape its depletion layer. However, important considerations and suggestion has to be done. Chips like MALTA2 are inherently very fragile, and working with them might not be adequate to pave the way to such an application. Implementing modifications on simpler devices like bare diodes may give better insight on how laser induced modification can shape the depletion layer of a pn junction, and how they affect the free carriers lifetime. In addition, in the next chapter5.3 a different, but complementing technique is presented and it will be shown how it is possible to experimentally study the shape of the depletion layer of a silicon based chip.

5.3 Two Photon Absorption-Transient Current Technique

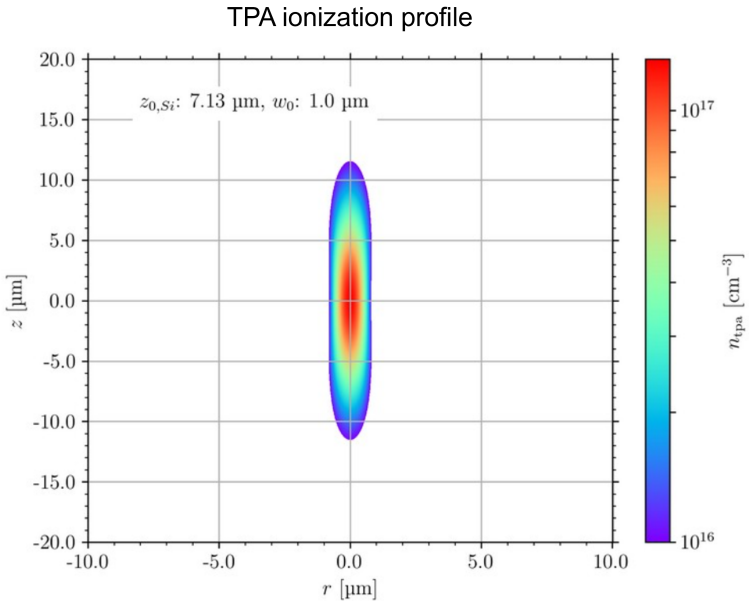

Figure 5.8: The simulation of the ionization profile generated with Two Photon Absorption of the 430 fs pulse is reported [38]. The density profile of free carriers produced around the focal spot is represented in the picture. [Figure from private communication with S. Pape (2023), TU Dortmund/CERN.]

The technique that follows is called Two Photon Absorption-Transient Current Technique, TPA-TCT for short, where the TPA is exploited to simulate the inner signals of a silicon based chip. It is not a simulation but an actual measurement, which makes it such

a promising technique. It is a non-destructive 3D scan of the signal response of a solid state detector. Normal edge-TCT only gives a 2D scan and the response is the convolution of the signal from all depths z in the sensor. So it is much more difficult to extract information. Multi-photon absorption in silicon is a second order process 1.1 that is unlocked at high fluence regimes. The fluence is defined as the optical energy delivered per unit area, and it is position dependent meaning that it depends on the beam profile. This is the reason why to achieve this effect it is required to have pulsed lasers to be highly focused in the sample, in this case with an objective with NA=0.55. The ionization profile of a single pulse is shown in Figure 5.8. It shows the density profile of free carriers produced around the focal spot. The produced free carriers make up for the signal that can be recorder by the chip. Consequently, the laser can be used to simulate high energy ionizing particles, and to test sub-pixel volumes of the chip individually and reliably.

5.3.1 TPA-TCT setup

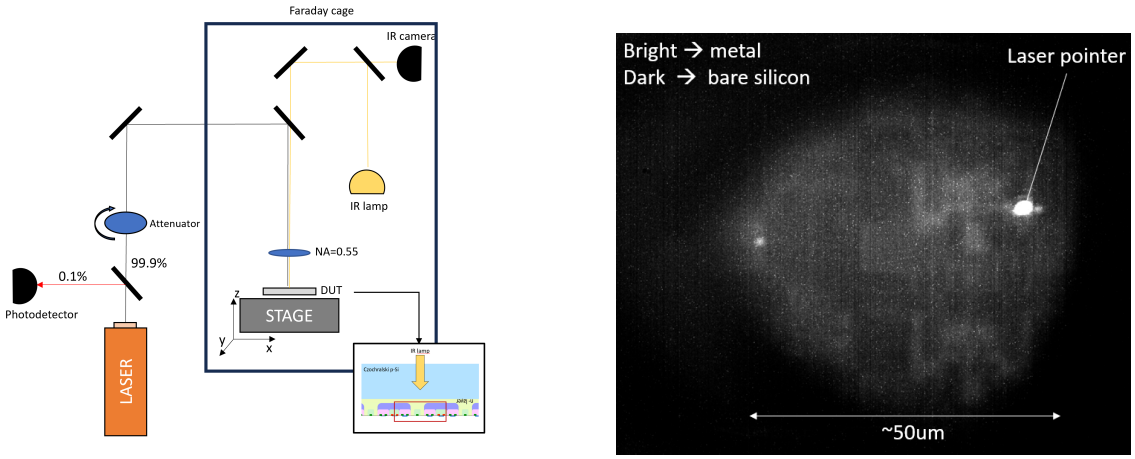

(a) (b)

Figure 5.9: (a) The TPA-TCT setup is composed by a ”laser system”, a ”control system” (photodetector), a ”monitoring system” (IR lamp and camera), and a ”delivery system” (all the rest). (b) IR camera view of the back metallized layer of MALTA2. The laser pointer is aligned with the pulsed laser to show the area under test.

During my stay at CERN we came in contact with a laboratory within the EP-DT-SSD

group that works with a laser setup similar to the one previously presented. It is composed by a laser system, a control system, a delivery system, and a monitoring system. The laser system produces a pulse with central wavelength 1.5 µm, pulse duration 430 fs, energy per pulse in the order of some pico Joules, and repetition rate f_{rep} tunable between 1 Hz to 8.2 MHz. The control system allows to keep under control the status of the output by extracting a fraction of the output beam from the laser system with a beam splitter, and reading it with a photodetector. The delivery system presents an attenuator based on a round continuously variable metallic neutral density filter to control the pulse energy to deliver to the DUT. At last, the monitoring system has been implemented to control in real time the aiming position of the laser on the DUT.

Monitoring system

The monitoring system is implemented in a fashion that would be desirable for the setup at NTNU as it would unlock the mentioned required precision in the x-y position. To monitor the aiming position of the pulsed laser, the optics is implemented with a He-Ne CW laser aligned along the same path as the main beam that shoots on the DUT. The position is then observed with an infrared InGaAs camera, again aligned with the optics, such that it receives the light reflected from the DUT. The DUT is also illuminated with an IR light source, which highlights the metallic features of the DUT making them bright; in addition, laser induced modifications should appear with a different contrast compared to the background because of the different refractive index.
The implementation of these monitoring features in the NTNU's setup would elevate the feasibility of high precision processing. Moreover, the implementation of another infrared camera at the side of the sample, thus looking at the sample cross section would allow the real time analysis of the sample processing. Even thought, it is important to state that the standard procedure to study the laser induced modifications requires to polish the sample down to the laser modifications to make them visible as shadow spots when illuminating the sample from the other side with IR light. Moving the focal spot inside the modified sample to cross the path of other innermost modifications did not allow their observation in the current homemade setup. Nevertheless, a specific imaging system for this applica-

tion might be built. Another reason to incorporate a cross-section imaging system into the setup is related to the high-precision stage movement used in NTNU's delivery system. Given the programmable stage movement, it would be possible to use it to perform an automatic scan of the sample (after polishing) that pictures every group of modifications, and after proper analysis suggests the best parameters to write in that particular sample. At the moment, the same analysis is performed manually as described in chapter 2.2. As a proof of concept, it was developed a script that takes images from the homemade IR microscope of a processed sample and returns the experimental position of the modifications for different values of pulse power, focal depth and aberration correction (see chapter 2.3.1). The implementation of such a system would speed up the process of finding the best writing parameters and would make it more reliable and free from human error in the data taking.

As a last note, it must be mentioned that as always it is for every tabletop experiment design, the space to be optimized is limited and not all the suggestions could be implemented altogether. Nevertheless, the improvements that they could bring given their relatively low monetary cost may be worth consideration.

5.3.2 MALTA2 setup requirements

Recalling the data acquisition mechanism of MALTA2 in Section5.1.3, we can now sharpen the description of the setup to effectively implement it in the TPA-TCT setup:

1. The chip is mounted on a PCB that presents an aperture to let the laser enter freely from the silicon side of MALTA2. It is mounted on the moving stage of the TPA-TCT setup through a 3D printed holder to keep the chip in the region of the focal spot defined by the delivery system optics.

2. The FPGA is connected to the PCB and to the PC. It requires a trigger signal to be sure that the recorded signals are real signals instead of noisy events. In fact, we record all noise just the same as real signals. However, we only read out 500 ns of data to the FIFO when a trigger arrives. If a noise trigger occurs at that time by accident, then it will be in the data as well. We just made sure to mask the noisiest

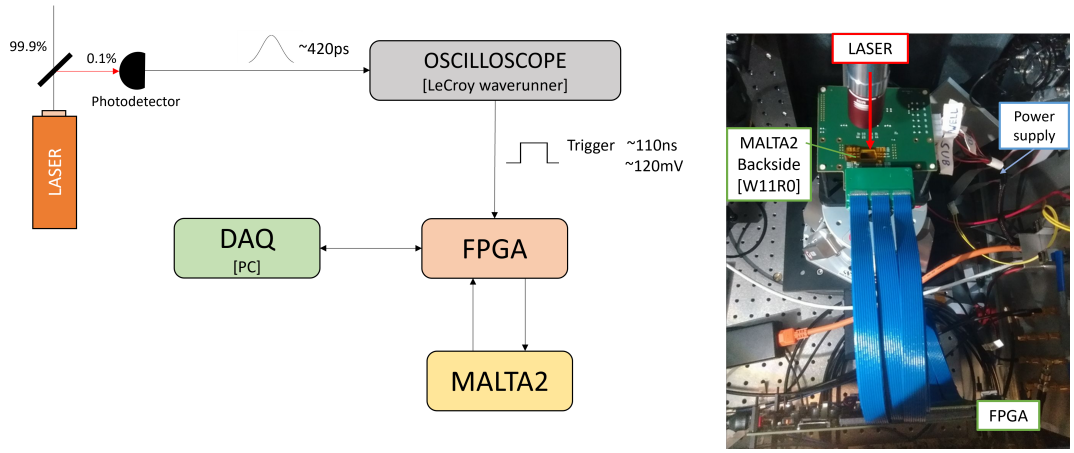

(a) (b)

Figure 5.10: (a) MALTA2 setup requirement. (b) MALTA2 setup within the Faraday cage of the TPA-TCT setup.

pixels on the matrix so that the chances of this happening are extremely low.

3. The working voltages of MALTA2 and of the FPGA are supplied with a PL303QMD from TTI.

4. A feed through for cables connects the FPGA and the MALTA2 carrier PCB to the PC outside of the Faraday cage.

5. As mentioned already, the oscilloscope receives the signal produced by the photodetector. The laser pulse ($\Delta\tau = 430\,\text{fs}$) is split at the output of the laser system and a fraction of it is read with the photodetector. The readout signal lasts around $\Delta\tau_{PD} = 420\,\text{ps}$ and has an amplitude of 100 mV. The oscilloscope triggers on this analogue pulse and sends out a digital pulse of $\Delta\tau_{trigger} = 110\,\text{ns}$ and with an amplitude of 500 mV. A 3dB attenuator is used to reduce the amplitude to roughly 120 mV before the signal is fed into the FPGA. The digital pulse of the oscilloscope has an additional delay of 18.3 ns compared to the original analogue signal. This delay can be compensated for by the configurable trigger delay at the shift register of the FPGA.

5.3.3 First measurements

As a first set of measurements, we wanted to test if it is possible to discriminate the boundaries between different pixels, and to find any difference in the time it would take for free carriers induced at different depths to reach the collection electrode. We decided to start from a random position and scan the matrix to completely cover at least fully one pixel. Subsequently, repeat the scan but with a different focal depth. In the data acquired from MALTA2 an event can be linked to the pixel that detected it, so it is possible to tell the position in the pixel matrix that the laser is aiming at. Note that an event can trigger two pixels at a time if the generated charge is shared among them.

As a first step, a noise scan is performed for the whole pixel matrix of the chip to identify and mask noisy pixels. This is done while the laser is turned off. At this point the monitoring system allows to focus the laser near the metallic surface of MALTA2 so to be sure to produce the free carriers in the depletion layer of the chip. The feedback from the stage returns the x, y, and z positions in the stage coordinate system. Regarding the starting x-y position, the laser points to an unknown position on the pixel matrix since with an IR camera it is not possible to distinguish the pixel edges, even though it is possible to distinguish the periodic metallic features at the other side5.9b. The repetition rate of the laser was chosen to be 1 kHz in order to safely avoid multiple counting. To change position, the shutter of the laser is closed, the stage moved, and the shutter opened again. Now, the chip is manually[2] read out. When 10^4 events are taken, the acquisition process of MALTA2 is manually shut down. With steps of 10 µm, an arbitrary area of the pixel matrix is scanned. The second depth was scanned shifting the z position of the stage by Δz_{air} =20 µm that correspond to a shift of the focus inside the silicon chip of $\Delta z_{Si} = \Delta z_{Si} \cdot n_{si}$ =76 µm, given n_{Si} =3.8, for the used wavelength and intensity.

Results

For each position the data is condensed into an histogram where the bins have been filled with the ”pulse timing”, measured by MALTA2 (see Figure 5.11). The pulse timing is

[2]The data acquisition script is run by the operator from the PC.

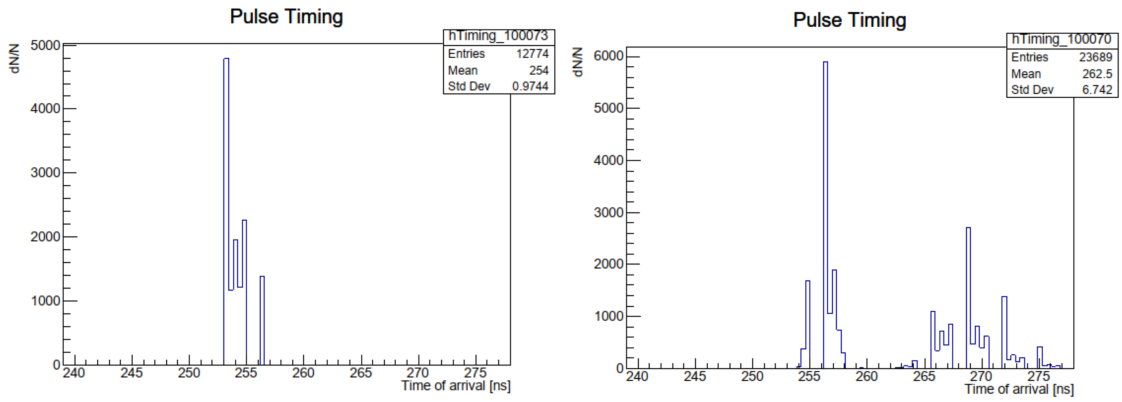

Figure 5.11: Counts on the y-axis. Pulse timing measurements shows that the peaks can appear as one or two peaks depending if only one or two pixels have recorded a signal. The data shows regular gaps that are probably related to the data acquisition mechanism of MALTA2.

given by the contribution of three time intervals:

1. Charge collection time: it is the time required for the ionized charges to reach the collection electrode. It is almost consistent in the whole depleted volume of the pixel, with a maximum delay of $\sim$2 ns between the pixel edge and the center of the pixel;

2. Time walk: it is time interval required by the signal generated by the collected charges to rise over the digital threshold of the pixel readout (see section 5.1.4);

3. Reading and processing time: it is the time required by the pixel to digitize the signal, and by the FPGA to read out and record the digital signal. It is constant and lasts $\sim$250 ns.

The charge collection time and the reading and processing time are constant for all signals, so the fluctuations in time among different pulse timings is given completely by the time walk. The reconstructed histograms can be divided into two categories, depending on if 1 or 2 peaks are visible. The histograms with 1 peak are related to the position that only trigger 1 pixel at a time, while 2 peaks are related to 2 triggered pixels. Efficiency helps

with the discrimination too. It is defined as the ratio between the number of recorded events and the number of sent triggers $N_{events}/N_{triggers}$. An efficiency of more than 100% can be caused by a single pulse triggering multiple pixels. In this case it is explained by the cloud of free carriers produced by one laser pulse splitting in two fractions, separately detected by the collection electrodes of adjacent pixels. If two pixels are activated with only one pulse the recorded events are two instead of only one. This behaviour is common at the volume around the edges between adjacent pixels (see section 5.1.4).

A common unexpected pattern to all the histograms is the division in 5+3 bins, where 5 bins are filled and 3 are empty. In addition, the 5 filled bins seem to possess constantly a smaller value in the even bins. This pattern arises when the bin division is kept at the lowest resolution available corresponding to Δt_{phase} =0.39 ns. This is an issue of the data acquisition process and could not be addressed while these measurements were done.

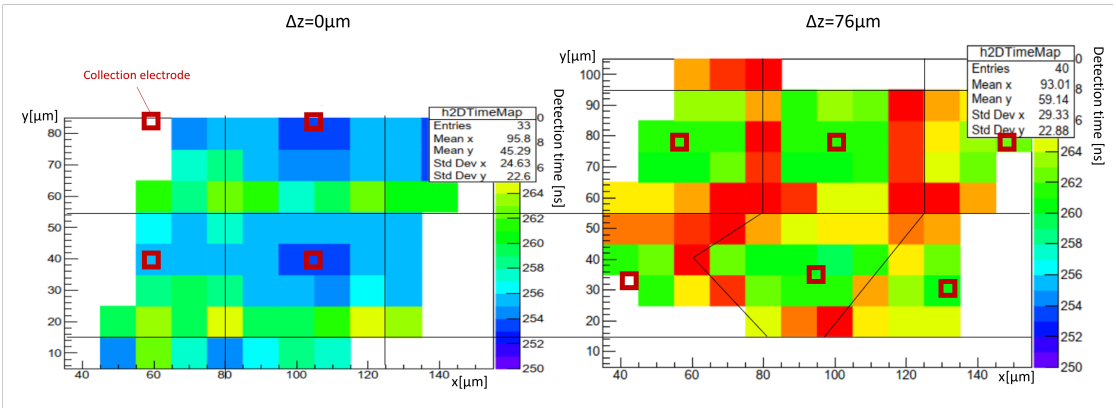

Figure 5.12: The colour scale in nanoseconds represents the average pulse timing of a signal (collection time + reading and processing time + time walk). The black lines represents the edges among different pixels and the red squares are placed in the identified position of the collection electrode. The Left: 2D time map of the scan performed with focus next to the metallic layer. Right: 2D time map of the scan performed with focus at depth Δz=76 μm.

For this first proof of concept, to generate a 2D time map of the scanned area, each position is assigned with the average pulse timing recorded for the 10^4 events. A 2D map of the scanned area is shown in Figure 5.12. From the acquired data it is also possible to point out which pixel have been triggered when shooting the laser in a certain position.

From this information the boundaries between the pixels have been traced as black lines. Notice how in certain areas the traces are not straight as one might expect. This is possibly due to the instability of the holder on with the PCB is mounted (see Figure5.10b). The PCB is fixed to the holder with plastic standoffs, and since the PCB is subjected to the tension of the stiff cable that connects it to the FPGA, it is possible that the standoffs are not perfectly straight. This tension on the PCB may produce some uncertainty in the position that is assigned to the chip which is read out as feedback from the moving stage and may not correspond reliably to the actual position of the laser on the chip. Nevertheless, it is evident how even a coarse scan with steps of 10 µm already shows the capability of the setup to distinguish the pixel boundaries and even the position of the collection diode (see Figure 5.12). At the boundaries a significantly larger signal arrival time relative to the trigger is observed compared to the center of a pixel.

Moreover, it is possible to compare the two scans taken next to the metal layer with focus at $\Delta z_0 = 0$ µm and the scan taken further away from the metal layer at focal depth of $\Delta z_1 = 76$ µm. The charges generated further from the circuitry require more time to be collected because they need to travel a longer distance. In addition, with an ionizing profile centered at a depth of 76 µm the charge is likely deposited outside the depletion layer. Therefore, the charge initially diffuses into an expanded charge cloud, extending until it makes contact with the depleted region. At this stage, the charge is spread out significantly, making it more easily redistributed among neighboring pixels. Since the ionizing profile of the pulse extends for 20 µm in silicon, it would be possible to perform many scans at different depths, and acquire more precision in measuring the depletion layer's shape.

5.3.4 Automatic scan

The approach just described was done completely manually to perform a proof of concept. However, the whole process was dependent on the operator presence and attention, and the need of an automatic scan was evident.

To perform an automatic scan the obstacles to overcome are a continuously running laser, and the impossibility to automatically close the shutter when changing position.

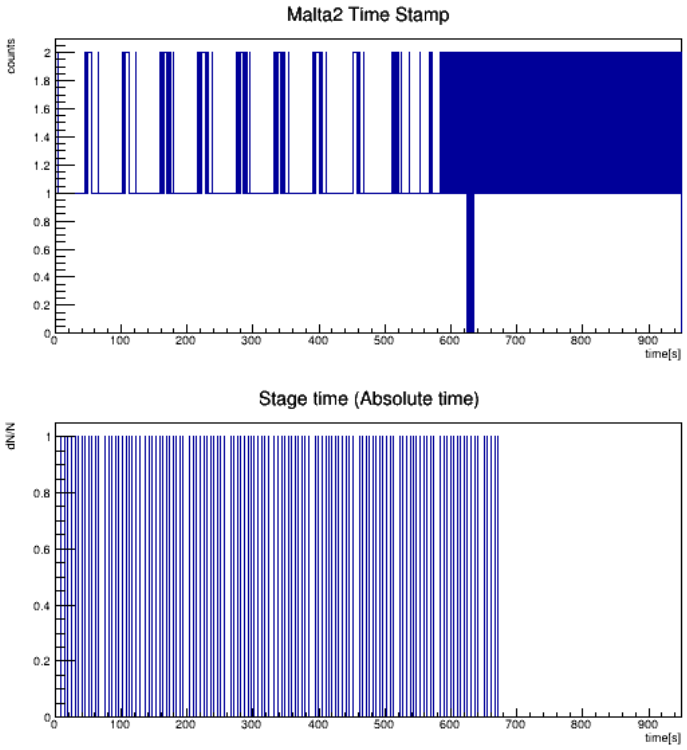

Figure 5.13: The counts are reported on the y-axis. (Bottom) Time stamp of the stage movement. A bin with value 1 indicates that the stage reached the n-th position at time t_n. (Top) Time stamp of the triggered events in in MALTA2. Starting from t_n, the next 10^3 events (until t_{n+999} included) are used to fill the pulse timing histogram of the corresponding n-th position.

The automation of the scanning process presents the challenge to operate a scan without a shutter. Since the laser runs continuously, the data is acquired also when the stage moves between different positions, requiring the correct assignment of the data to be performed after the measurements. The available shutter is in fact a safety feature that completely blocks the laser output, while for this application a controllable shutter at the MALTA2 input or at the trigger output would have been needed. Hence, with a continuously running laser, the correct assignment of the recorded signals to the right position was done exploiting the time stamp of the stage position. To make it clear, we have two types of time data:

1. The time at which the stage reaches a new position.

2. A trigger count $n_{trigger}$ and its frequency $f_{trigger}$. Since we know the order of recorded events and the frequency they are received at (the same as for the trigger), we can reconstruct the stream of data in time as $t_{MALTA2} = n_{trigger}/f_{trigger}$. This is valid under the condition that no signal is lost and that no noisy event is recorded.

To overlap the two timelines we only need a reference time for when the shutter opens. When opened, the shutter allows the trigger to reach the chip and the data acquisition begins. We finally have the correctly reconstructed and calibrated time of both the stage movement and the timestamp of the events. The trigger frequency this time was chosen to be 200 Hz, and the area was scanned in an 11×11 grid with steps of 2 µm, scanning an area of $20\times20\,\mu m^2$. The stage remains in the same position for 5 s to allow the acquisition of 10^3 events per point. So, for every time assigned to the position of the stage the next 10^3 events are assigned to that position. In this way we avoid all the events that are acquired during the stage movement.

Analysis

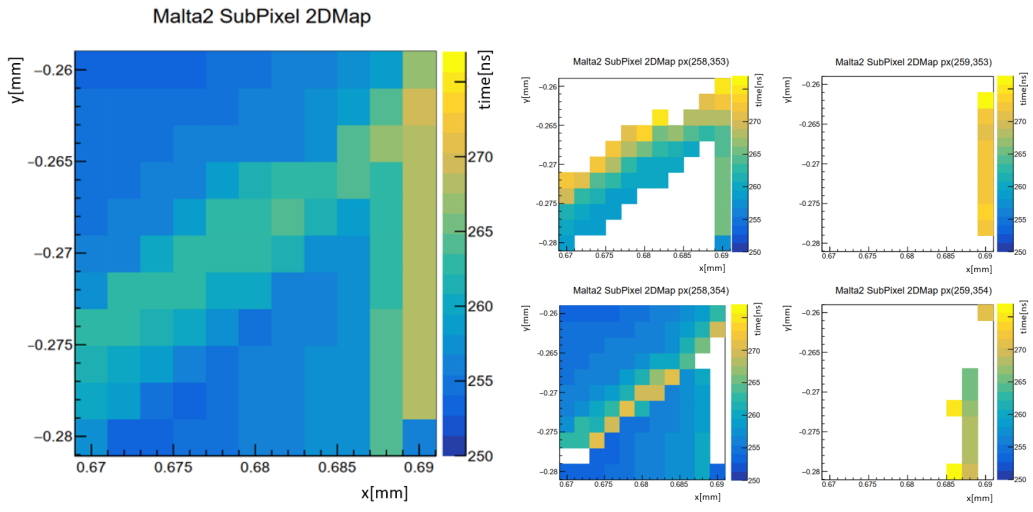

(a) (b)

Figure 5.14: The colour scale in nanoseconds represents the average pulse timing of a signal. (a) Automatic scan of MALTA2. (b) A distinction among the different triggered pixels is shown.

The first step of the analysis is the correct assignment of the acquired events to the correct position, as explained already. After the data taking, for each position we are left with an histogram of 10^3 events distributed in time. Each time represents the time it took to the free carriers to reach the readout with the trigger as a reference. So for example, a signal produced next to the collection diode are faster to be recorded then a signal at the edge of the pixel because the time walk is much larger. As for the previous scan, for a final result we want to map the collection time of the scanned area. Each position can be assigned with the average collection time; thus, producing the map presented in Figure5.14a. As done previously, we can also assign each event to the triggered pixel and obtain for each pixel a 2D map of the positions that trigger it, with the proper collection time. This map is difficult to interpret, since it does not show an evident edge between the triggered pixels. In fact, from the whole 2D map, it may seem that two pixels have been scanned with the border appearing diagonally. However, when looking at the 2D map of the single pixels separately (Figure5.14b), it looks like pixel (258,354) have been triggered during the whole scan, even when crossing what seems to be the diagonal border. As mentioned before, it is possible that the stiff cable that connects the PCB and the FPGA(Figure5.10b) is affecting the measured positions, but from the division into single pixels it seems like pixel (258,353) lays inside pixel (258,358). Of course, this is not possible, instead, it simply suggests that pixel (258,353) have been triggered with the laser aiming at those positions, with cause to be found in other sources of error. One way to assess the reasons is to retake the measurements in a different area of the matrix, and observe if the anomalous behaviour persists. Moreover, regarding the correct assignment of the position, it is possible to calibrate the real position from the recorded position, comparing the stage position of at least 4 distant points that lay in 4 different pixels with the position of these pixels within the pixel matrix.

This time, we want to perform an analysis with more effort in studying the double peaks in the time histograms (see Figure 5.11). For each position we have a time distribution of the events. One would expect it to have a well-defined peak and resembling a

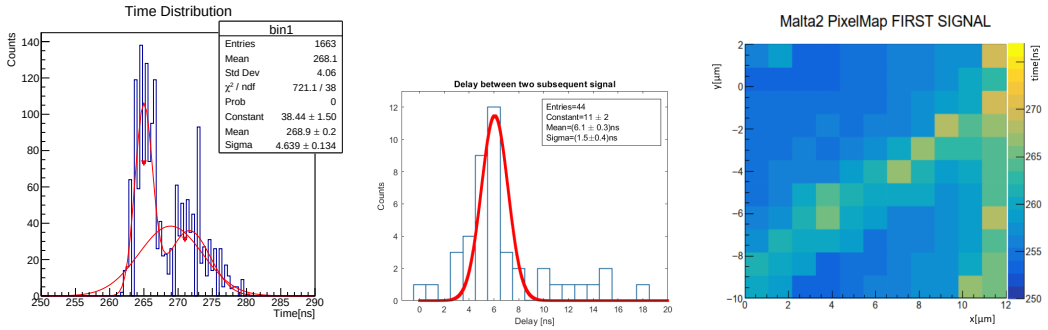

(a) (b) (c)

Figure 5.15: (a) Single and double Gaussian fit of the time histogram of (x,y) position (0.690,-0.278)mm. (b) Time delay between the two signals recorded at the pixel edges. (c) 2D map filled only with the fastest time response recorded.

Gaussian distribution[3]. So, to assign the average pulse timing to each position it is possible to perform a single or double Gaussian fit and take the fit with the lowest reduced χ^2_r as the most reliable. From such a fit it is possible to build a new 2D time map assigning to each position the central position of the first of the two Gaussian, i.e. the "first signal" . This allows to only consider the fastest pulse timing of MALTA2 for a given position. In fact, the second peak appears due to the readout mechanics of the 2x8 pixel group (see section 5.1.4). The results are summed up in Figure 5.15c. In addition, we can plot the time delay between the two Gaussian peaks (when present), as reported in Figure 5.15b, where the histogram was fitted with a Gaussian. The measured delay is centered at $6.1(3)$ ns with a standard deviation of $\sigma_{delay} = 1.5(4)$ ns.

5.3.5 Conclusions

The performed experiment was by itself a proof of concept to understand the capabilities and limitation of the characterization with TPA-TCT of MALTA2, and in general of any monolithic pixel detector. The results showed that it is possible to have an insight of the inner behaviour of the free carriers. These results can be compared to TCAD simulations

[3]Deep reasons behind a Gaussian distribution are not really given. It is assumed here that time fluctuations of the single event are random.

of the free carrier dynamics to further refine and enhance the characterization of the chip. The results obtained with the characterization of MALTA2 with TPA-TCT suggest TPA-TCT as a complementary technique to study the laser-induced defects produced with the NTNU's laser setup. The modification of a basic and less fragile electronic component, e.g. a diode, and its consequent characterization with TPA-TCT would deepen the understanding of the electronic and solid state properties of the laser-induced modifications, and the possibilities and limitations in shaping the depletion layer in silicon based chip.

Conclusions and Outlook

Ultrafast Laser Direct Writing (ULDW) has been proven to alter the lattice structure of monocrystalline silicon introducing defects that range from vacancies to clusters of vacancies. The precise nature of the defects is still under investigation. Nevertheless, we could demonstrate already now the usefulness of the results for creation of the following functional silicon devices:

1. Positronium BEC target. Here we could obtain particularly promising results as we could demonstrate for the first time how to create *hollow* volumes embedded in silicon that might have numerous applications besides the positronium BEC target. The modified volumes show high etching selectivity to HF-based etchant solutions. This selectivity allowed to produce subsurface open cavities $\sim$200 nm tall and some micrometers wide. These cavities are connected to the surface by a comb of nanochannels, that are capable of high e^+-Ps conversion. The procedure employed to produce these structures is reliable and reproducible. Further work on the refinement of a positronium target may pave the way for the production of the first purely leptonic Bose-Einstein condensate made of positronium atoms.

2. MALTA2 chip, where the final goal is increasing the sensitivity of the detector. At this stage, the direct processing with ULDW of the Depleted Monolithic Active Pixel Sensor MALTA2 has shown that metallized surfaces alter the behaviour of the laser propagation. The metallized surface reflected the beam causing secondary modifications in the chip introducing defects in the CMOS implants and breaking the chip. The inherently fragile structure of MALTA2 did not allow to explore the capabilities of ULDW to shape the depletion layer of the chip. The implantation of laser defects in simpler devices, like bare diodes, may give better insight on how ULDW can shape the depletion layer of a pn junction, and how laser defects affect the free carriers lifetime. Furthermore, Two Photon Absorption-Transient Current Technique (TPA-TCT) is suggested as a complementary tool in this research. TPA-

TCT can be used to directly study electronic and solid state properties of the laser-induced defects, and the possibilities and limitations in shaping the depletion layer in silicon based chip. Direct measurements obtained with TPA-TCT can be compared to TCAD simulations of the free carrier dynamics to further refine and enhance the characterization of the chip.

Bibliography

[1] Roland Richter, Nikolai Tolstik, and Irina T. Sorokina. “In-bulk silicon processing with ultrashort pulsed lasers: three-photon-absorption versus two-photon-absorption”. In: *High-Brightness Sources and Light-driven Interactions* (2018), MW4C.2. DOI: 10.1364/MICS.2018.MW4C.2. URL: https://opg.optica.org/abstract.cfm?URI=MICS-2018-MW4C.2.

[2] N. Tolstik et al. “Single-pulse Laser Induced Buried Defects in Silicon Written by Ultrashort-pulse Laser at 2.1 um”. In: *Conference on Lasers and Electro-Optics*. Optica Publishing Group, 2022, AM4I.8. DOI: 10.1364/CLEO_AT.2022.AM4I.8. URL: https://opg.optica.org/abstract.cfm?URI=CLEO_AT-2022-AM4I.8.

[3] Margaux Chanal et al. “Crossing the threshold of ultrafast laser writing in bulk silicon”. In: *Nature Communications* 8.1 (Oct. 2017), p. 773. ISSN: 2041-1723. DOI: 10.1038/s41467-017-00907-8.

[4] Tokel O et al. “In-chip microstructures and photonic devices fabricated by nonlinear laser lithography deep inside silicon.” In: *Nature Photonics* 11.10 (Oct. 2017), pp. 639–645. DOI: 10.1038/s41566-017-0004-4.

[5] Roland A. Richter et al. “Sub-surface modifications in silicon with ultra-short pulsed lasers above 2 µm”. In: *J. Opt. Soc. Am. B* 37.9 (Sept. 2020), pp. 2543–2556. DOI: 10.1364/JOSAB.396074. URL: https://opg.optica.org/josab/abstract.cfm?URI=josab-37-9-2543.

[6] E V Zavedeev, V V Kononenko, and V I Konov. “Delocalization of femtosecond laser radiation in crystalline Si in the mid-IR range”. In: *Laser Physics* 26.1 (Dec. 2015), p. 016101. DOI: 10.1088/1054-660X/26/1/016101. URL: https://dx.doi.org/10.1088/1054-660X/26/1/016101.

[7] Katherine C. Phillips et al. “Ultrafast laser processing of materials: a review”. In: *Adv. Opt. Photon.* 7.4 (Dec. 2015), pp. 684–712. DOI: 10.1364/AOP.7.000684. URL: https://opg.optica.org/aop/abstract.cfm?URI=aop-7-4-684.

[8] R. A. Richter V. L. Kalashnikov A. Rudenkov I. T. Sorokina N. Tolstik and E. Sorokin. “Ultrafast Mid-IR Lasers: Making a Difference in Science and Industry.” In: *Proceedings of the VII International Symposium on Ultrafast Dynamics and Metastability 2022, 6 - 10 June 2022, Crete, Greece* (June 2022), pp. 84–85.

[9] B. L. Sopori. “A New Defect Etch for Polycrystalline Silicon”. In: *Journal of The Electrochemical Society* 131.3 (Mar. 1984), p. 667. DOI: 10.1149/1.2115670. URL: https://dx.doi.org/10.1149/1.2115670.

[10] Richard J Mathar. “Refractive index of humid air in the infrared: model fits”. In: *J. Opt. A: Pure Appl. Opt.* 9.5 (2007).

[11] E. Shkondin et al. “Large-scale high aspect ratio Al-doped ZnO nanopillars arrays as anisotropic metamaterials”. In: *Opt. Mater. Express* 7 (2017), pp. 1606–1627.

[12] Peter J. Schultz and K. G. Lynn. “Interaction of positron beams with surfaces, thin films, and interfaces”. In: *Rev. Mod. Phys.* 60 (3 July 1988), pp. 701–779. DOI: 10.1103/RevModPhys.60.701. URL: https://link.aps.org/doi/10.1103/RevModPhys.60.701.

[13] S. Mariazzi et al. “High positronium yield and emission into the vacuum from oxidized tunable nanochannels in silicon”. In: *Phys. Rev. B* 81 (23 June 2010), p. 235418. DOI: 10.1103/PhysRevB.81.235418. URL: https://link.aps.org/doi/10.1103/PhysRevB.81.235418.

[14] S. Mariazzi, A. Salemi, and R. S. Brusa. “Positronium cooling into nanopores and nanochannels by phonon scattering”. In: *Phys. Rev. B* 78 (8 Aug. 2008), p. 085428. DOI: 10.1103/PhysRevB.78.085428. URL: https://link.aps.org/doi/10.1103/PhysRevB.78.085428.

[15] Sebastiano Mariazzi, Paolo Bettotti, and Roberto S. Brusa. “Positronium Cooling and Emission in Vacuum from Nanochannels at Cryogenic Temperature”. In: *Phys. Rev. Lett.* 104 (24 June 2010), p. 243401. DOI: 10.1103/PhysRevLett.104.243401. URL: https://link.aps.org/doi/10.1103/PhysRevLett.104.243401.

[16] Claude Amsler et al. “Pulsed production of antihydrogen”. In: *Communications Physics* 4.1 (Feb. 2021), p. 19. ISSN: 2399-3650. DOI: 10.1038/s42005-020-00494-z. URL: https://doi.org/10.1038/s42005-020-00494-z.

[17] S. Aghion et al. “Laser excitation of the n=3 level of positronium for antihydrogen production”. In: *Phys. Rev. A* 94 (1 July 2016), p. 012507. DOI: 10.1103/PhysRevA.94.012507. URL: https://link.aps.org/doi/10.1103/PhysRevA.94.012507.

[18] D. Krasnický et al. “Cross section for Rydberg antihydrogen production via charge exchange between Rydberg positroniums and antiprotons in a magnetic field”. In: *Phys. Rev. A* 94 (2 Aug. 2016), p. 022714. DOI: 10.1103/PhysRevA.94.022714. URL: https://link.aps.org/doi/10.1103/PhysRevA.94.022714.

[19] David B. Cassidy. “Experimental progress in positronium laser physics”. In: *The European Physical Journal D* 72.3 (Mar. 2018), p. 53. ISSN: 1434-6079. DOI: 10.1140/epjd/e2018-80721-y. URL: https://doi.org/10.1140/epjd/e2018-80721-y.

[20] P. M. Platzman and A. P. Mills. “Possibilities for Bose condensation of positronium”. In: *Phys. Rev. B* 49 (1 Jan. 1994), pp. 454–458. DOI: 10.1103/PhysRevB.49.454. URL: https://link.aps.org/doi/10.1103/PhysRevB.49.454.

[21] Nagendra Nath Mondal. “Challenges and advances of positronium Bose-Einstein condensation”. In: *AIP Advances* 9.5 (May 2019), p. 055310. ISSN: 2158-3226. DOI: 10.1063/1.5090916. URL: https://doi.org/10.1063/1.5090916.

[22] Fuentes-Garcia Melina et al. Asaro Marcus X. Herrera Steven. “Conditions for obtaining positronium Bose–Einstein condensation in a micron-sized cavity”. In: *The European Physical Journal D* 76 (6 June 2022), pp. 1434–6079. DOI: 10.1140/epjd/s10053-022-00427-1. URL: https://doi.org/10.1140/epjd/s10053-022-00427-1.

[23] L. T. Glöggler et al. “Positronium Laser Cooling via the 1^3S-2^3P Transition with a Broadband Laser Pulse”. In: *Phys. Rev. Lett.* 132 (8 Feb. 2024), p. 083402. DOI: 10.1103/PhysRevLett.132.083402. URL: https://link.aps.org/doi/10.1103/PhysRevLett.132.083402.

[24] K. Shu et al. *Laser cooling of positronium*. 2023. arXiv: 2310.08761 [physics.atom-ph].

[25] L. V. Jørgensen et al. “New Source of Dense, Cryogenic Positron Plasmas”. In: *Phys. Rev. Lett.* 95 (2 July 2005), p. 025002. DOI: 10.1103/PhysRevLett.95.025002. URL: https://link.aps.org/doi/10.1103/PhysRevLett.95.025002.

[26] D W Fitzakerley et al. “Electron-cooled accumulation of 4×10^9 *positrons for production and storage of antihydrogen atoms*”. In: *Journal of Physics B: Atomic, Molecular and Optical Physics* 49.6 (Feb. 2016), p. 064001. DOI: 10.1088/0953-4075/49/6/064001. URL: https://dx.doi.org/10.1088/0953-4075/49/6/064001.

[27] Martin A. Green. “Self-consistent optical parameters of intrinsic silicon at 300K including temperature coefficients”. In: *Solar Energy Materials and Solar Cells* 92.11 (2008), pp. 1305–1310. ISSN: 0927-0248. DOI: https://doi.org/10.1016/j.solmat.2008.06.009. URL: https://www.sciencedirect.com/science/article/pii/S0927024808002158.

[28] Nieminen R. M. Valkealahti S. “Monte-Carlo calculations of keV electron and positron slowing down in solids”. In: *Applied Physics A* 32 (2 Oct. 1983). DOI: 10.1007/BF00617834. URL: https://doi.org/10.1007/BF00617834.

[29] S Pirollo et al. “Radiation damage on p-type silicon detectors”. In: *Nuclear Instruments and Methods in Physics Research Section A: Accelerators, Spectrometers, Detectors and Associated Equipment* 426.1 (1999), pp. 126–130. ISSN: 0168-9002. DOI: https://doi.org/10.1016/S0168-9002(98)01480-6. URL: https://www.sciencedirect.com/science/article/pii/S0168900298014806.

[30] Z Li. “Radiation damage effects in Si materials and detectors and rad-hard Si detectors for SLHC”. In: *Journal of Instrumentation* 4.03 (Mar. 2009), P03011. DOI: 10.1088/1748-0221/4/03/P03011. URL: https://dx.doi.org/10.1088/1748-0221/4/03/P03011.

[31] O. Bisi, Stefano Ossicini, and L. Pavesi. “Porous silicon: a quantum sponge structure for silicon based optoelectronics”. In: *Surface Science Reports* 38.1 (2000), pp. 1–126. ISSN: 0167-5729. DOI: https://doi.org/10.1016/S0167-5729(99)00012-6. URL: https://www.sciencedirect.com/science/article/pii/S0167572999000126.

[32] R. S. Brusa et al. “Formation of vacancy clusters and cavities in He-implanted silicon studied by slow-positron annihilation spectroscopy”. In: *PHYSICAL REVIEW B* 61.15 (2000), pp. 10154–10166. ISSN: 1098-0121. DOI: 10.1103/PhysRevB.61.10154.

[33] S. Mariazzi et al. “Forward emission of positronium from nanochanneled silicon membranes”. In: *Phys. Rev. B* 105 (11 Mar. 2022), p. 115422. DOI: 10.1103/PhysRevB.105.115422. URL: https://link.aps.org/doi/10.1103/PhysRevB.105.115422.

[34] H. Pernegger et al. “MALTA-Cz: a radiation hard full-size monolithic CMOS sensor with small electrodes on high-resistivity Czochralski substrate”. In: *Journal of Instrumentation* 18.09 (Sept. 2023), P09018. DOI: 10.1088/1748-0221/18/09/P09018. URL: https://dx.doi.org/10.1088/1748-0221/18/09/P09018.

[35] S Meroli, D Passeri, and L Servoli. “Energy loss measurement for charged particles in very thin silicon layers”. In: *Journal of Instrumentation* 6.06 (June 2011), P06013. DOI: 10.1088/1748-0221/6/06/P06013. URL: https://dx.doi.org/10.1088/1748-0221/6/06/P06013.

[36] Vladimir Cindro et al. “Radiation damage in p-type silicon irradiated with neutrons and protons”. In: *Nuclear Instruments and Methods in Physics Research Section A: Accelerators, Spectrometers, Detectors and Associated Equipment*

599.1 (2009), pp. 60–65. ISSN: 0168-9002. DOI: https://doi.org/10.1016/j.nima.2008.11.007. URL: https://www.sciencedirect.com/science/article/pii/S0168900208015969.

[37] I. Mandić et al. “Neutron irradiation test of depleted CMOS pixel detector prototypes”. In: *Journal of Instrumentation* 12.02 (Feb. 2017), P02021. DOI: 10.1088/1748-0221/12/02/P02021. URL: https://dx.doi.org/10.1088/1748-0221/12/02/P02021.

[38] Moritz Wiehe et al. “Development of a Tabletop Setup for the Transient Current Technique Using Two-Photon Absorption in Silicon Particle Detectors”. In: *IEEE Transactions on Nuclear Science* 68.2 (2021), pp. 220–228. DOI: 10.1109/TNS.2020.3044489.

[39] I. B. Larsen. “On the characterisation and improvement of a positron-positronium converter”. In: *Semester project* Norwegian University of Science and Technology (NTNU) (2014).

[40] Roberto Sennen Brusa et al. “Porosity of Low-κ Materials Studied by Slow Positron Beam”. In: *Acta Physica Polonica A* 107.4 (2005), pp. 702–711.

Appendix

A Positron annihilation spectroscopy

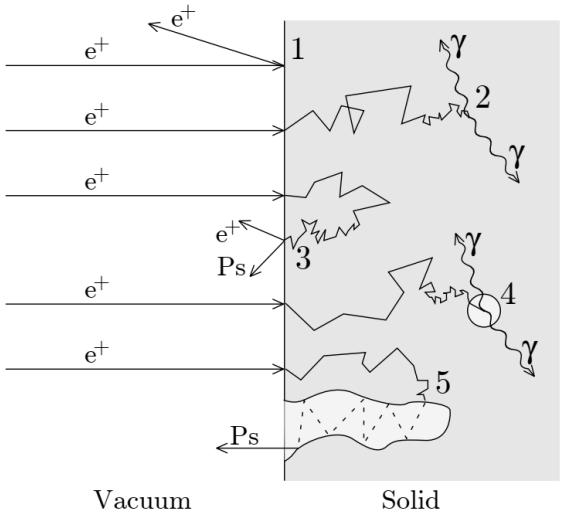

Figure 16: Schematic overview of some of the different processes that positrons can undergo when implanted into solids [39].

- Back-scattering of high-energy positrons.
- Thermalization, diffusion and eventually annihilation in the material.
- Re-emission of either positrons or positronium after thermalization and diffusion.
- Annihilation of a positron or positronium atom trapped in a defect.
- Formation of positronium in defects that are connected to the surface, and subsequent escape into a vacuum.

Slow positron measurements are performed by moderating positrons emitted by a radioactive source and implanting them into the sample to analyse. At the Antimatter Laboratory of UNITN the kinetic energy of the slow positron beam ranges from few eV to 20 keV, resulting in a maximum positron implantation depth of 2 μm in crystalline silicon.

Positron annihilation spectroscopy (PAS) operates based on the principle that a positrons in matter will eventually undergo annihilation due to the interaction with an electron with subsequent emission of gamma rays that can be detected. Within the material each positron can undergo different processes depending on the local material topology that it encounters, and among these processes positronium can form. A summary of these processes is presented in Figure 16. When implanted into a solid, positrons begin a diffusive motion in the bulk, thus thermalizing with the material. For solids containing free electrons (such as metals or semiconductors), the implanted positrons annihilate rapidly with them emitting 2γ, each at 511keV, with broadening of the detected peak due to the momentum of the involved electron. If the solid is a perfect crystal, the positrons can annihilate with high-momentum core electrons. If voids (mono or multi vacancy defects) are available, positrons will reside in them and annihilate in 2γ mainly with low-momentum valence electrons. For insulators such as SiO_2, implanted positrons interact with electrons in the material to form positronium. At the surface, the conversion is favoured due to positron trap, and the Ps is prone to be emitted outside the bulk. The positronium itself can diffuse in the bulk where the interaction with valence electrons produces a 2γ emission. Or, it can reach the surface and be emitted outside the sample, or in an open cavity. In a vacuum (either outside the sample or in an open cavity) the Ps[4] can live up to 142 n sec and it annihilate in 3γ. This result in a high count rate in the valley to the left of the 511 keV peak. With proper calibration, it is possible to extract the absolute value of positrons annihilating as Ps through 3γ emissions.

The main parameters extrapolated from the annihilation spectrum of the implanted slow positron beam are: S-parameter and $F_3\gamma$-parameter.

S-parameter defines the proportion of annihilation of positrons with low-momentum electrons, i.e. valence electrons, as a function of the implantation energy. It is defined as the ratio of the counts in the central part of the 511 keV peak over the total area of the peak. It is closely linked to the concentration of defects in a material: high defect concentration means high probability of annihilation with low-momentum electrons resulting in high S values; while, low defect concentration is linked to high probability of annihilation with

[4]The o-Ps.

core electrons resulting in a low S value.

$F_{3\gamma}$-parameter defines the fraction of implanted positrons at energy E forming o-Ps and annihilating by 3γ. It is calculated as the ratio of the 2γ annihilations in the 511 keV annihilation peak and the 3γ annihilations in the area below the peak. It requires a calibration crystal that can give 0% and 100% Ps yield. In the performed experimental conditions a Ge crystal held at 1000 K was used for calibration [40].

B Resistivity measurements

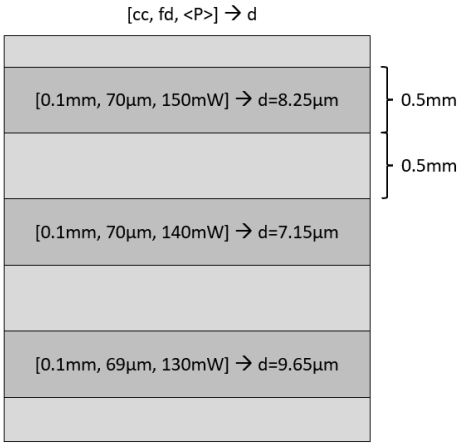

Figure 17: Implantation scheme for resistivity measurements.

A sample of p-type Si wafer with resistivity 0.17-0.23 Ω cm, from producer values, was implanted with ULDW to measure the change in resistivity caused by the laser writing. In Figure 17 it is presented the implantation scheme and the laser parameters used. A 2D layer of single pulse modifications was implanted in sections of 0.5 mm few micrometres under the surface. The choice of the small size and of a single layer was dictated by time limitations, to write one layer of 0.5 mm it takes 20 min. The sample was then measured with a 4 point probe, we found no difference thorough both samples, with values that correspond to resistivity [0.18, 0.19, 0.20](1) Ohm cm, perfectly in accordance with the specifications given by the manufacturer [0.17-0.23]Ohm cm. Assuming a thickness of the modified volume of 1 µm, over a 300 µm thick sample, it is the 0.3% of the overall

thickness, evidently too little to be discriminated. Most probably the overall unmodified volume was masking the contribution of the written part. So, to be sure that the injected current flows in the modified volume it is necessary to produce samples with large modified volume. A different approach might be to make a whole volume 1mm wide, spanning the whole thickness of the sample. In this case the resistivity might change sensibly.

C Sopori etching

Samples to etch are bits of crystalline silicon wafer, modified with Ultrafast Laser Direct Writing and mechanically polished down to expose the laser induced modifications on the surface.

The required solutions are:

1. RCA1: $H_2O : H_2O_2 : NH_4OH = 5 : 1 : 1$
2. 5% HF
3. Solution A: $HNO_3 : HF =: 1$
4. Sopori: $HF : CH_3COOH : HNO_3 = 36 : 15 : 2$

A first cleaning procedure is required to eliminate any organic residue on the surface:

1. RCA1 warmed to 70 °C
2. sample in RCA1 for 10 min
3. sample rinsed in DI-water (twice)

The etching procedure is the following:

1. Sample in 5% HF for 3 min
2. Sample in Sopori for 25 sec
3. Sample in Solution A for 5 sec
4. Sample rinsed in DI-water (twice)

5. Sample rinsed with ethanol (spray bottle)

6. Dispose the chemicals

Acknowledgments

The Research Council of Norway is acknowledged for the support to the Norwegian Micro- and Nano-Fabrication Facility, NorFab, project #295864, as well as NFR project #326503 (MIR).

The work on the laser processing was conducted in close collaboration with Maksim Demesh, PhD candidate at NTNU, and in collaboration with the whole team of researchers within the MIR project. The characterization of MALTA2 with TPA-TCT was made possible through collaboration with Sebastian Pape, PhD candidate at TU Dortmund/CERN.

Working on this master's thesis has been a life-changing experience. Life and physics have never been so intimately connected, and I have treasured every one of those moments.

Irina, from the very beginning you gave me trust, and this would never have been possible without your support.

Florian, I know it was your job to teach me, but your passion and kindness went well beyond.

Sebastiano, ci vediamo lunedì in lab? I hope to be at the level of the trust you have placed in me.

To all the friends I made along the way...

...e agli amici che sono stati le mie "vecchie rocce".

Ad Anna, la poesia della mia vita.

A mia madre, a mia sorella, a mio padre.

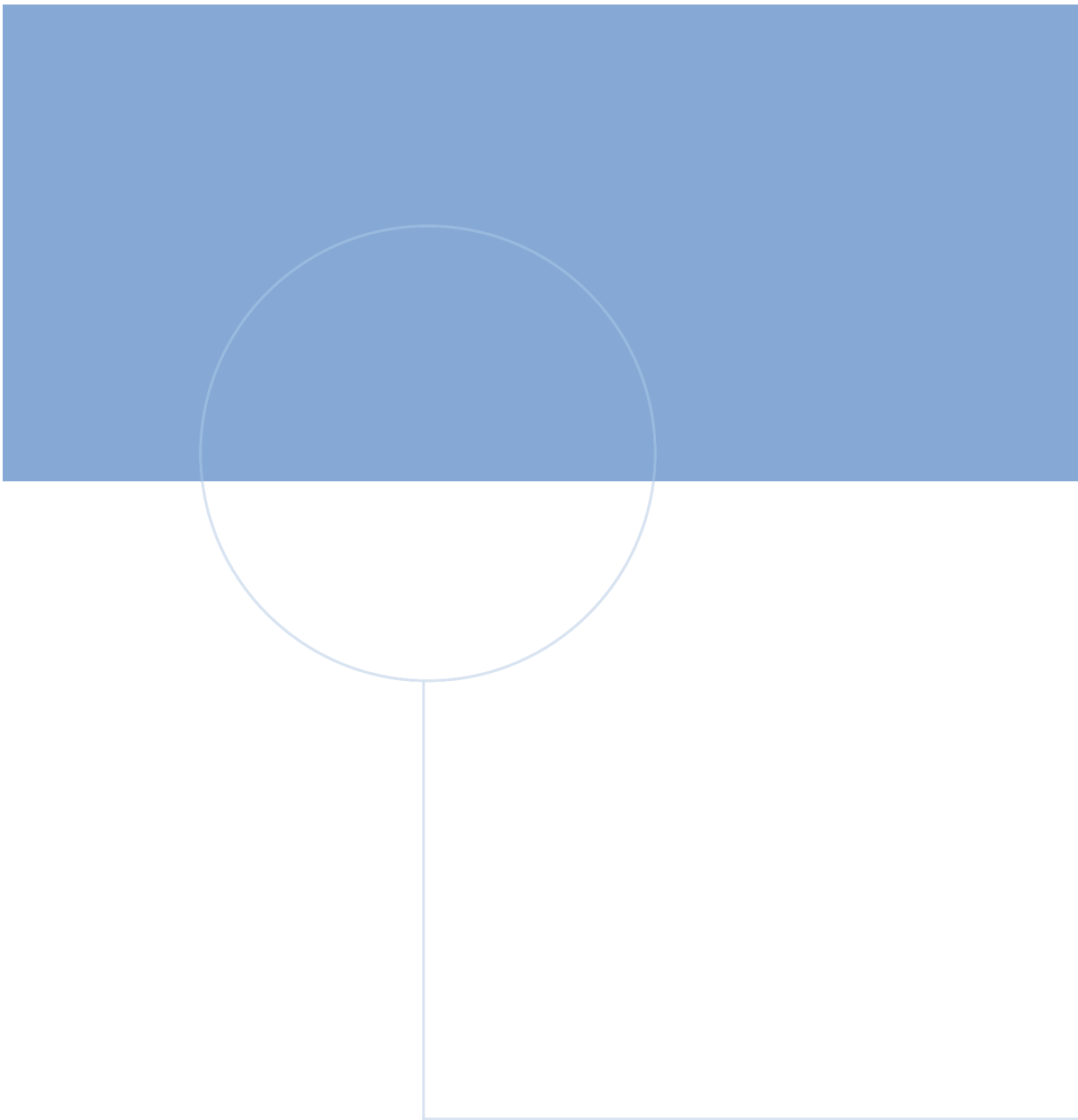

NTNU
Norwegian University of
Science and Technology

UNIVERSITÀ
DI TRENTO

CERN